Production of charged pions, kaons, and protons in e^+e^- annihilations into hadrons at $\sqrt{s} = 10.54$ GeV

J. P. Lees,[1] V. Poireau,[1] V. Tisserand,[1] E. Grauges,[2] A. Palano,[3a,3b] G. Eigen,[4] B. Stugu,[4] D. N. Brown,[5] L. T. Kerth,[5] Yu. G. Kolomensky,[5] M. Lee,[5] G. Lynch,[5] H. Koch,[6] T. Schroeder,[6] C. Hearty,[7] T. S. Mattison,[7] J. A. McKenna,[7] R. Y. So,[7] A. Khan,[8] V. E. Blinov,[9] A. R. Buzykaev,[9] V. P. Druzhinin,[9] V. B. Golubev,[9] E. A. Kravchenko,[9] A. P. Onuchin,[9] S. I. Serednyakov,[9] Yu. I. Skovpen,[9] E. P. Solodov,[9] K. Yu. Todyshev,[9] A. N. Yushkov,[9] D. Kirkby,[10] A. J. Lankford,[10] M. Mandelkern,[10] C. Buchanan,[11] B. Hartfiel,[11] B. Dey,[12] J. W. Gary,[12] O. Long,[12] G. M. Vitug,[12] C. Campagnari,[13] M. Franco Sevilla,[13] T. M. Hong,[13] D. Kovalskyi,[13] J. D. Richman,[13] C. A. West,[13] A. M. Eisner,[14] W. S. Lockman,[14] A. J. Martinez,[14] B. A. Schumm,[14] A. Seiden,[14] D. S. Chao,[15] C. H. Cheng,[15] B. Echenard,[15] K. T. Flood,[15] D. G. Hitlin,[15] P. Ongmongkolkul,[15] F. C. Porter,[15] R. Andreassen,[16] Z. Huard,[16] B. T. Meadows,[16] M. D. Sokoloff,[16] L. Sun,[16] P. C. Bloom,[17] W. T. Ford,[17] A. Gaz,[17] U. Nauenberg,[17] J. G. Smith,[17] S. R. Wagner,[17] R. Ayad,[18,†] W. H. Toki,[18] B. Spaan,[19] K. R. Schubert,[20] R. Schwierz,[20] D. Bernard,[21] M. Verderi,[21] S. Playfer,[22] D. Bettoni,[23a] C. Bozzi,[23a] R. Calabrese,[23a,23b] G. Cibinetto,[23a,23b] E. Fioravanti,[23a,23b] I. Garzia,[23a,23b] E. Luppi,[23a,23b] L. Piemontese,[23a] V. Santoro,[23a] R. Baldini-Ferroli,[24] A. Calcaterra,[24] R. de Sangro,[24] G. Finocchiaro,[24] S. Martellotti,[24] P. Patteri,[24] I. M. Peruzzi,[24,‡] M. Piccolo,[24] M. Rama,[24] A. Zallo,[24] R. Contri,[25a,25b] E. Guido,[25a,25b] M. Lo Vetere,[25a,25b] M. R. Monge,[25a,25b] S. Passaggio,[25a] C. Patrignani,[25a,25b] E. Robutti,[25a] B. Bhuyan,[26] V. Prasad,[26] M. Morii,[27] A. Adametz,[28] U. Uwer,[28] H. M. Lacker,[29] P. D. Dauncey,[30] U. Mallik,[31] C. Chen,[32] J. Cochran,[32] W. T. Meyer,[32] S. Prell,[32] A. E. Rubin,[32] A. V. Gritsan,[33] N. Arnaud,[34] M. Davier,[34] D. Derkach,[34] G. Grosdidier,[34] F. Le Diberder,[34] A. M. Lutz,[34] B. Malaescu,[34] P. Roudeau,[34] A. Stocchi,[34] G. Wormser,[34] D. J. Lange,[35] D. M. Wright,[35] J. P. Coleman,[36] J. R. Fry,[36] E. Gabathuler,[36] D. E. Hutchcroft,[36] D. J. Payne,[36] C. Touramanis,[36] A. J. Bevan,[37] F. Di Lodovico,[37] R. Sacco,[37] G. Cowan,[38] J. Bougher,[39] D. N. Brown,[39] C. L. Davis,[39] A. G. Denig,[40] M. Fritsch,[40] W. Gradl,[40] K. Griessinger,[40] A. Hafner,[40] E. Prencipe,[40] R. J. Barlow,[41,§] G. D. Lafferty,[41] E. Behn,[42] R. Cenci,[42] B. Hamilton,[42] A. Jawahery,[42] D. A. Roberts,[42] R. Cowan,[43] D. Dujmic,[43] G. Sciolla,[43] R. Cheaib,[44] P. M. Patel,[44,*] S. H. Robertson,[44] P. Biassoni,[45a,45b] N. Neri,[45a] F. Palombo,[45a,45b] L. Cremaldi,[46] R. Godang,[46,‖] P. Sonnek,[46] D. J. Summers,[46] X. Nguyen,[47] M. Simard,[47] P. Taras,[47] G. De Nardo,[48a,48b] D. Monorchio,[48a,48b] G. Onorato,[48a,48b] C. Sciacca,[48a,48b] M. Martinelli,[49] G. Raven,[49] C. P. Jessop,[50] J. M. LoSecco,[50] K. Honscheid,[51] R. Kass,[51] J. Brau,[52] R. Frey,[52] N. B. Sinev,[52] D. Strom,[52] E. Torrence,[52] E. Feltresi,[53a,53b] M. Margoni,[53a,53b] M. Morandin,[53a] M. Posocco,[53a] M. Rotondo,[53a] G. Simi,[53a] F. Simonetto,[53a,53b] R. Stroili,[53a,53b] S. Akar,[54] E. Ben-Haim,[54] M. Bomben,[54] G. R. Bonneaud,[54] H. Briand,[54] G. Calderini,[54] J. Chauveau,[54] Ph. Leruste,[54] G. Marchiori,[54] J. Ocariz,[54] S. Sitt,[54] M. Biasini,[55a,55b] E. Manoni,[55a] S. Pacetti,[55a,55b] A. Rossi,[55a,55b] C. Angelini,[56a,56b] G. Batignani,[56a,56b] S. Bettarini,[56a,56b] M. Carpinelli,[56a,56b,¶] G. Casarosa,[56a,56b] A. Cervelli,[56a,56b] F. Forti,[56a,56b] M. A. Giorgi,[56a,56b] A. Lusiani,[56a,56c] B. Oberhof,[56a,56b] E. Paoloni,[56a,56b] A. Perez,[56a] G. Rizzo,[56a,56b] J. J. Walsh,[56a] D. Lopes Pegna,[57] J. Olsen,[57] A. J. S. Smith,[57] R. Faccini,[58a,58b] F. Ferrarotto,[58a] F. Ferroni,[58a,58b] M. Gaspero,[58a,58b] L. Li Gioi,[58a] G. Piredda,[58a] C. Bünger,[59] S. Christ,[59] O. Grünberg,[59] T. Hartmann,[59] T. Leddig,[59] H. Schröder,[59,*] C. Voß,[59] R. Waldi,[59] T. Adye,[60] E. O. Olaiya,[60] F. F. Wilson,[60] S. Emery,[61] G. Hamel de Monchenault,[61] G. Vasseur,[61] Ch. Yèche,[61] F. Anulli,[62] D. Aston,[62] D. J. Bard,[62] J. F. Benitez,[62] C. Cartaro,[62] M. R. Convery,[62] J. Dorfan,[62] G. P. Dubois-Felsmann,[62] W. Dunwoodie,[62] M. Ebert,[62] R. C. Field,[62] B. G. Fulsom,[62] A. M. Gabareen,[62] M. T. Graham,[62] T. Haas,[62] T. Hadig,[62] C. Hast,[62] W. R. Innes,[62] P. Kim,[62] M. L. Kocian,[62] D. W. G. S. Leith,[62] P. Lewis,[62] D. Lindemann,[62] B. Lindquist,[62] S. Luitz,[62] V. Luth,[62] H. L. Lynch,[62] D. B. MacFarlane,[62] D. R. Muller,[62] H. Neal,[62] S. Nelson,[62] M. Perl,[62] T. Pulliam,[62] B. N. Ratcliff,[62] A. Roodman,[62] A. A. Salnikov,[62] R. H. Schindler,[62] J. Schwiening,[62] A. Snyder,[62] D. Su,[62] M. K. Sullivan,[62] J. Va'vra,[62] A. P. Wagner,[62] W. F. Wang,[62] W. J. Wisniewski,[62] M. Wittgen,[62] D. H. Wright,[62] H. W. Wulsin,[62] V. Ziegler,[62] W. Park,[63] M. V. Purohit,[63] R. M. White,[63,**] J. R. Wilson,[63] A. Randle-Conde,[64] S. J. Sekula,[64] M. Bellis,[65] P. R. Burchat,[65] T. S. Miyashita,[65] E. M. T. Puccio,[65] M. S. Alam,[66] J. A. Ernst,[66] R. Gorodeisky,[67] N. Guttman,[67] D. R. Peimer,[67] A. Soffer,[67] S. M. Spanier,[68] J. L. Ritchie,[69] A. M. Ruland,[69] R. F. Schwitters,[69] B. C. Wray,[69] J. M. Izen,[70] X. C. Lou,[70] F. Bianchi,[71a,71b] F. De Mori,[71a,71b] A. Filippi,[71a] D. Gamba,[71a,71b] S. Zambito,[71a,71b] L. Lanceri,[72a,72b] L. Vitale,[72a,72b] F. Martinez-Vidal,[73] A. Oyanguren,[73] P. Villanueva-Perez,[73] H. Ahmed,[74] J. Albert,[74] Sw. Banerjee,[74] F. U. Bernlochner,[74] H. H. F. Choi,[74] G. J. King,[74] R. Kowalewski,[74] M. J. Lewczuk,[74] T. Lueck,[74] I. M. Nugent,[74] J. M. Roney,[74] R. J. Sobie,[74] N. Tasneem,[74] T. J. Gershon,[75] P. F. Harrison,[75] T. E. Latham,[75] H. R. Band,[76] S. Dasu,[76] Y. Pan,[76] R. Prepost,[76] and S. L. Wu[76]

(*BABAR* Collaboration)

[1]*Laboratoire d'Annecy-le-Vieux de Physique des Particules (LAPP), Université de Savoie, CNRS/IN2P3, F-74941 Annecy-Le-Vieux, France*
[2]*Departament ECM, Facultat de Fisica, Universitat de Barcelona, E-08028 Barcelona, Spain*
[3a]*INFN Sezione di Bari, I-70126 Bari, Italy*
[3b]*Dipartimento di Fisica, Università di Bari, I-70126 Bari, Italy*
[4]*University of Bergen, Institute of Physics, N-5007 Bergen, Norway*
[5]*Lawrence Berkeley National Laboratory and University of California, Berkeley, California 94720, USA*
[6]*Ruhr Universität Bochum, Institut für Experimentalphysik 1, D-44780 Bochum, Germany*
[7]*University of British Columbia, Vancouver, British Columbia, V6T 1Z1 Canada*
[8]*Brunel University, Uxbridge, Middlesex UB8 3PH, United Kingdom*
[9]*Budker Institute of Nuclear Physics SB RAS, Novosibirsk 630090, Russia*
[10]*University of California at Irvine, Irvine, California 92697, USA*
[11]*University of California at Los Angeles, Los Angeles, California 90024, USA*
[12]*University of California at Riverside, Riverside, California 92521, USA*
[13]*University of California at Santa Barbara, Santa Barbara, California 93106, USA*
[14]*University of California at Santa Cruz, Institute for Particle Physics, Santa Cruz, California 95064, USA*
[15]*California Institute of Technology, Pasadena, California 91125, USA*
[16]*University of Cincinnati, Cincinnati, Ohio 45221, USA*
[17]*University of Colorado, Boulder, Colorado 80309, USA*
[18]*Colorado State University, Fort Collins, Colorado 80523, USA*
[19]*Fakultät Physik, Technische Universität Dortmund, D-44221 Dortmund, Germany*
[20]*Technische Universität Dresden, Institut für Kern- und Teilchenphysik, D-01062 Dresden, Germany*
[21]*Laboratoire Leprince-Ringuet, Ecole Polytechnique, CNRS/IN2P3, F-91128 Palaiseau, France*
[22]*University of Edinburgh, Edinburgh EH9 3JZ, United Kingdom*
[23a]*INFN Sezione di Ferrara, I-44122 Ferrara, Italy*
[23b]*Dipartimento di Fisica e Scienze della Terra, Università di Ferrara, I-44122 Ferrara, Italy*
[24]*INFN Laboratori Nazionali di Frascati, I-00044 Frascati, Italy*
[25a]*INFN Sezione di Genova, I-16146 Genova, Italy*
[25b]*Dipartimento di Fisica, Università di Genova, I-16146 Genova, Italy*
[26]*Indian Institute of Technology Guwahati, Guwahati, Assam 781 039, India*
[27]*Harvard University, Cambridge, Massachusetts 02138, USA*
[28]*Universität Heidelberg, Physikalisches Institut, Philosophenweg 12, D-69120 Heidelberg, Germany*
[29]*Humboldt-Universität zu Berlin, Institut für Physik, Newtonstrasse 15, D-12489 Berlin, Germany*
[30]*Imperial College London, London SW7 2AZ, United Kingdom*
[31]*University of Iowa, Iowa City, Iowa 52242, USA*
[32]*Iowa State University, Ames, Iowa 50011-3160, USA*
[33]*Johns Hopkins University, Baltimore, Maryland 21218, USA*
[34]*Laboratoire de l'Accélérateur Linéaire, IN2P3/CNRS et Université Paris-Sud 11, Centre Scientifique d'Orsay, B. P. 34, F-91898 Orsay Cedex, France*
[35]*Lawrence Livermore National Laboratory, Livermore, California 94550, USA*
[36]*University of Liverpool, Liverpool L69 7ZE, United Kingdom*
[37]*Queen Mary, University of London, London, E1 4NS, United Kingdom*
[38]*Royal Holloway and Bedford New College, University of London, Egham, Surrey TW20 0EX, United Kingdom*
[39]*University of Louisville, Louisville, Kentucky 40292, USA*
[40]*Johannes Gutenberg-Universität Mainz, Institut für Kernphysik, D-55099 Mainz, Germany*
[41]*University of Manchester, Manchester M13 9PL, United Kingdom*
[42]*University of Maryland, College Park, Maryland 20742, USA*
[43]*Massachusetts Institute of Technology, Laboratory for Nuclear Science, Cambridge, Massachusetts 02139, USA*
[44]*McGill University, Montréal, Québec H3A 2T8, Canada*
[45a]*INFN Sezione di Milano, I-20133 Milano, Italy*
[45b]*Dipartimento di Fisica, Università di Milano, I-20133 Milano, Italy*
[46]*University of Mississippi, University, Mississippi 38677, USA*
[47]*Université de Montréal, Physique des Particules, Montréal, Québec H3C 3J7, Canada*
[48a]*INFN Sezione di Napoli, I-80126 Napoli, Italy*
[48b]*Dipartimento di Scienze Fisiche, Università di Napoli Federico II, I-80126 Napoli, Italy*
[49]*NIKHEF, National Institute for Nuclear Physics and High Energy Physics, NL-1009 DB Amsterdam, The Netherlands*
[50]*University of Notre Dame, Notre Dame, Indiana 46556, USA*

[51]Ohio State University, Columbus, Ohio 43210, USA

[52]University of Oregon, Eugene, Oregon 97403, USA

[53a]INFN Sezione di Padova, I-35131 Padova, Italy

[53b]Dipartimento di Fisica, Università di Padova, I-35131 Padova, Italy

[54]Laboratoire de Physique Nucléaire et de Hautes Energies, IN2P3/CNRS, Université Pierre et Marie Curie-Paris6,
Université Denis Diderot-Paris7, F-75252 Paris, France

[55a]INFN Sezione di Perugia, I-06100 Perugia, Italy

[55b]Dipartimento di Fisica, Università di Perugia, I-06100 Perugia, Italy

[56a]INFN Sezione di Pisa, I-56127 Pisa, Italy

[56b]Dipartimento di Fisica, Università di Pisa, I-56127 Pisa, Italy

[56c]Scuola Normale Superiore di Pisa, I-56127 Pisa, Italy

[57]Princeton University, Princeton, New Jersey 08544, USA

[58a]INFN Sezione di Roma, I-00185 Roma, Italy

[58b]Dipartimento di Fisica, Università di Roma La Sapienza, I-00185 Roma, Italy

[59]Universität Rostock, D-18051 Rostock, Germany

[60]Rutherford Appleton Laboratory, Chilton, Didcot, Oxon OX11 0QX, United Kingdom

[61]CEA, Irfu, SPP, Centre de Saclay, F-91191 Gif-sur-Yvette, France

[62]SLAC National Accelerator Laboratory, Stanford, California 94309, USA

[63]University of South Carolina, Columbia, South Carolina 29208, USA

[64]Southern Methodist University, Dallas, Texas 75275, USA

[65]Stanford University, Stanford, California 94305-4060, USA

[66]State University of New York, Albany, New York 12222, USA

[67]Tel Aviv University, School of Physics and Astronomy, Tel Aviv 69978, Israel

[68]University of Tennessee, Knoxville, Tennessee 37996, USA

[69]University of Texas at Austin, Austin, Texas 78712, USA

[70]University of Texas at Dallas, Richardson, Texas 75083, USA

[71a]INFN Sezione di Torino, I-10125 Torino, Italy

[71b]Dipartimento di Fisica Sperimentale, Università di Torino, I-10125 Torino, Italy

[72a]INFN Sezione di Trieste, I-34127 Trieste, Italy

[72b]Dipartimento di Fisica, Università di Trieste, I-34127 Trieste, Italy

[73]IFIC, Universitat de Valencia-CSIC, E-46071 Valencia, Spain

[74]University of Victoria, Victoria, British Columbia V8W 3P6, Canada

[75]Department of Physics, University of Warwick, Coventry CV4 7AL, United Kingdom

[76]University of Wisconsin, Madison, Wisconsin 53706, USA

Inclusive production cross sections of $\pi^\pm$, $K^\pm$ and $p/\bar{p}$ per hadronic e^+e^- annihilation event are measured at a center-of-mass energy of 10.54 GeV, using a relatively small sample of very high quality data from the *BABAR* experiment at the PEP-II *B*-factory at the SLAC National Accelerator Laboratory. The drift chamber and Cherenkov detector provide clean samples of identified $\pi^\pm$, $K^\pm$, and $p/\bar{p}$ over a wide range of momenta. Since the center-of-mass energy is below the threshold to produce a $B\bar{B}$ pair, with *B* a bottom-quark meson, these data represent a pure $e^+e^- \rightarrow q\bar{q}$ sample with four quark flavors, and are used to test QCD predictions and hadronization models. Combined with measurements at other energies, in particular at the Z^0 resonance, they also provide precise constraints on the scaling properties of the hadronization process over a wide energy range.

*Deceased.

†Present address: University of Tabuk, Tabuk 71491, Saudi Arabia.

‡Also at Dipartimento di Fisica, Università di Perugia, Perugia, Italy.

§Present address: University of Huddersfield, Huddersfield HD1 3DH, United Kingdom.

‖Present address: University of South Alabama, Mobile, Alabama 36688, USA.

¶Also at Università di Sassari, Sassari, Italy.

**Present address: Universidad Técnica Federico Santa Maria, 2390123 Valparaiso, Chile.

I. INTRODUCTION

The production of hadrons from energetic quarks and gluons in high-energy collisions is well described by qualitative models, but there are few quantitative theoretical predictions. Detailed experimental information about hadron production allows the confining property of the strong interaction to be probed. An empirical understanding of confinement is important to the interpretation of much current and future high-energy data, in which the observable products of interactions and decays of heavy particles,

known and yet to be discovered, appear as jets of hadrons. Measurements involving identified hadrons probe the influence on this process of hadron masses and quantum numbers such as strangeness, baryon number, and spin.

The process $e^+e^- \rightarrow q\bar{q} \rightarrow$ hadrons is understood to proceed through three stages. In the first stage, the quark (q) and antiquark ($\bar{q}$) "fragment" via the radiation of gluons (g), each of which can radiate further gluons or split into a $q\bar{q}$ pair. This process is, in principle, calculable in perturbative quantum chromodynamics (QCD), and there are calculations for up to four final-state partons, corresponding to second order in the strong coupling α_S [1], where by "parton" we mean either a quark or a gluon. In addition, leading-order calculations exist for as many as six partons [2], as well as calculations to all orders in α_S in the modified leading logarithm approximation (MLLA) [3]. There are also "parton shower" Monte Carlo simulations [4] that include an arbitrary number of $q \rightarrow qg$, $g \rightarrow gg$ and $g \rightarrow q\bar{q}$ branchings, with probabilities determined up to next-to-leading logarithm level.

In the second stage, these partons "hadronize," or transform into "primary" hadrons, a step that is not understood quantitatively. The ansatz of local parton-hadron duality (LPHD) [3], that inclusive distributions of primary hadrons are the same up to a scale factor as those for partons, allows MLLA QCD to predict properties of distributions of the dimensionless variable $\xi = -\ln x_p$ for different hadrons. Here, $x_p = 2p^*/E_{CM}$ is the scaled momentum, and p^* and E_{CM} are the hadron momentum and the e^+e^- energy, respectively, in the e^+e^- center-of-mass (CM) frame. Predictions include the shape of the ξ distribution and its dependence on hadron mass and E_{CM}. At sufficiently high x_p, perturbative QCD has also been used to calculate the E_{CM} dependence of the x_p distributions [5].

In the third stage, unstable primary hadrons decay into more stable particles, which can reach detector elements. Although proper lifetimes and decay branching fractions have been measured for many hadron species, these decays complicate fundamental measurements because many of the stable particles are decay products rather than primary hadrons. Previous measurements at e^+e^- colliders [6] indicate that decays of vector mesons, strange baryons, and decuplet baryons produce roughly two thirds of the stable particles; scalar and tensor mesons and radially excited baryons have also been observed and contribute additional secondary hadrons. Ideally one would measure every hadron species and distinguish primary hadrons from decay products on a statistical basis. A body of knowledge could be assembled by reconstructing increasingly heavy states and subtracting their known decay products from the measured rates of lighter hadrons. The measurement of the stable charged hadrons constitutes a first step in such a program.

There are several phenomenological models of hadronic jet production. To model the parton production stage, the

HERWIG 5.8 [7], JETSET 7.4 [8] and UCLA 4.1 [9] event generators rely on combinations of first-order matrix elements and parton-shower simulations. For the hadronization stage, the HERWIG model splits the gluons produced in the first stage into $q\bar{q}$ pairs, combines these quarks and antiquarks locally to form colorless "clusters," and decays the clusters into primary hadrons. The JETSET model represents the color field between the partons by a "string," and breaks the string according to an iterative algorithm into several pieces, each corresponding to a primary hadron. The UCLA model generates whole events according to weights derived from phase space and Clebsch-Gordan coefficients. Each model contains free parameters controlling various aspects of the hadronization process, whose values have been tuned to reproduce data from e^+e^- annihilations. With a large number of parameters, JETSET has the potential to model many hadron species in detail, whereas UCLA and HERWIG seek a more global description with fewer parameters, including only one or two that control the relative rates of different species.

The scaling properties, or E_{CM} dependences, of hadron production are of particular interest. Since the process is governed by QCD, it is expected to be scale invariant, i.e. distributions of x_p should be independent of E_{CM} except for the effects of hadron masses/phase space and the running of α_S. The quark flavor composition varies with E_{CM}, and may also have substantial effects. Mass effects are observed to be large unless $x_p \gg m_h/E_{CM}$, where m_h is the mass of the hadron in question, although current experimental precision is limited at lower energies. At high x_p, the expected scaling violations have been calculated [5] and found to be consistent with available data, but experimental precision is limited for specific hadron species. The scaling violation for inclusive charged tracks has been used to extract α_S under a number of assumptions about the dependence on event flavor and particle type [10]. Improved precision at 10.54 GeV would provide stringent tests of such assumptions and more robust measurements of α_S.

The production of the charged hadrons $\pi^{\pm}$, $K^{\pm}$, and $p/\bar{p}$ has been studied in e^+e^- annihilations at E_{CM} values of 10 GeV [11], 29 GeV [12], 34 and 44 GeV [13], 58 GeV [14], 91 GeV [15–18], and at several points in the range 130–200 GeV [19]. Recently, Belle has measured $\pi^{\pm}$ and $K^{\pm}$ production at 10.52 GeV [20]. Results for 91 GeV, near the Z^0 pole, include precise measurements in inclusive hadronic events, as well as measurements for separated quark flavors, quark and gluon jets, and leading particles [21,22]. The higher- and lower-energy measurements are, however, limited in precision and x_p coverage. Improved precision over the full x_p range at 10.54 GeV would probe the large scaling violations in detail and provide sensitive new tests of QCD calculations and hadronization models.

In this article, we present measurements of the inclusive normalized production cross sections of charged pions,

kaons, and protons per $e^+e^- \rightarrow q\bar{q}$ event. We use 0.91 fb^{-1} of data recorded by the *BABAR* detector at the PEP-II storage ring at SLAC in March, 2002, at a CM energy of 10.54 GeV. This is a small fraction of the *BABAR* "off-resonance" data, recorded during a period dedicated to the delivery of stable beams and constant luminosity. The detector experienced relatively low backgrounds and ran in its most efficient configuration, which was not changed in this period. In parallel, we analyze 3.6 fb^{-1} of data recorded at the $\Upsilon(4S)$ resonance (10.58 GeV) during the remainder of this period, February–April, 2002. This "on-resonance" sample provides independent, stringent systematic checks, and the combined samples provide data-derived calibrations of the tracking and particle identification performance. The uncertainties on the results are dominated by systematic contributions.

The detector and event selection are described in Secs. II and III. The selection of high quality charged tracks and their identification as pions, kaons or protons is discussed in Sec. IV. The measurement of the cross sections, including corrections for the effects of backgrounds, detector efficiency and resolution, and the boost of the e^+e^- system in the *BABAR* laboratory frame, are described in Sec. V. The results are compared with previous results and with the predictions of QCD and hadronization models in Sec. VI, and are summarized in Sec. VII.

II. THE *BABAR* DETECTOR

The e^+e^- system is boosted in the *BABAR* laboratory frame by $\beta\gamma = 0.56$ along the e^- beam direction. We call this direction "forward," $+z$, and denote quantities in the e^+e^- CM frame with an asterisk, and those in the laboratory frame with a subscript "lab." For example, p^* denotes the magnitude of a particle's momentum in the CM frame and θ^* its angle with respect to the e^- beam direction, and p_{lab} and θ_{lab} denote the corresponding quantities in the laboratory frame. For $e^+e^- \rightarrow q\bar{q}$ events at $E_{CM} = 10.54$ GeV, the maximum p^* value is $E_{CM}/2 = 5.27$ GeV/c, but the maximum p_{lab} value depends on polar angle, with values of 3.8 GeV/c at $\cos\theta_{lab} = -0.8$ and 7 GeV/c at $\cos\theta_{lab} = +0.9$. Thus, particles with a given p^* value have different p_{lab} values in different regions of the detector, and are measured with different efficiencies and systematic uncertainties.

The *BABAR* detector is described in detail in Ref. [23]. In this analysis, we use charged tracks measured in the silicon vertex tracker (SVT) and the drift chamber (DCH), and identified in the DCH and the detector of internally reflected Cherenkov light (DIRC). We also use energy deposits measured in the CsI(Tl) crystal calorimeter (EMC) to identify electron tracks and construct quantities used in the event selection. These subdetectors operate in a 1.5 T solenoidal magnetic field.

The SVT comprises five double-sided layers of strip detectors, each of which measures a coordinate along (z)

and azimuthally around (ϕ) the beam axis. The DCH includes 40 layers of axial and stereo wires. Their combined resolution is $\sigma_{p_t}/p_t = 0.45\% \oplus (0.13\% \cdot p_t[\text{GeV}/c])$, where p_t is the momentum transverse to the beam axis. The DCH measures ionization energy loss (dE/dx) with a resolution of 8%.

The DIRC [24] consists of 144 fused silica radiator bars that guide Cherenkov photons to an expansion volume filled with water and equipped with 10,752 photomultiplier tubes. It covers the polar angle range $-0.8 < \cos\theta_{lab} < 0.9$. The refractive index of 1.473 corresponds to Cherenkov thresholds of 0.13, 0.48 and 0.87 GeV/c for $\pi^\pm$, $K^\pm$ and $p/\bar{p}$, respectively. The Cherenkov angles of detected photons are measured with an average resolution of 10.2 mrad. Tracks with very high p_{lab} yield an average of 20 detected photons at $\cos\theta_{lab} = 0$, rising to 65 photons at the most forward and backward angles.

The EMC comprises 5,760 CsI(Tl) crystals in a projective geometry that measure clusters of energy with a resolution of $\sigma_E/E = 1.85\% \oplus (2.32\%/\sqrt[4]{E[\text{GeV}]})$. An algorithm identifies electrons using track momentum combined with EMC measurements of energy and shower shape. It has better than 95% efficiency for $p_{lab} > 0.2$ GeV/c, and hadron misidentification rates of up to 1% for $p_{lab} < 0.5$ GeV/c and at most 0.1% for higher momenta.

III. HADRONIC EVENT SELECTION

The event selection is optimized for low bias across the hadron momentum spectra and $e^+e^- \rightarrow q\bar{q}$ event multiplicity distribution, while minimizing backgrounds from other physics processes and beam-wall and beam-gas interactions. After fitting each combination of three or more reconstructed charged tracks to a common vertex, we require

(1) at least three charged tracks and one good vertex, where a good vertex has a χ^2 confidence level above 0.01;
(2) the good vertex with the highest track multiplicity to lie within 5 mm of the beam axis, and within 5 cm of the center of the collision region in z;
(3) the second Fox-Wolfram moment [25] to be less than 0.9;
(4) the sum of the energies of the charged tracks and unassociated neutral clusters E_{tot} to be in the range 5–14 GeV;
(5) the polar angle of the event thrust [26] axis in the CM frame to satisfy $|\cos\theta^*_{thrust}| < 0.8$;
(6) the track with the highest p_{lab} not to be identified as an electron in events with fewer than six tracks, and neither of the two highest-p_{lab} tracks to be identified as an electron in events with only three tracks.

Criteria 3 and 6 reject leptonic events, $e^+e^- \rightarrow e^+e^-$, $\mu^+\mu^-$, and $\tau^+\tau^-$. Criteria 4 and 5 ensure that the event is well contained within the sensitive volume of the

detector, resulting in smaller corrections and lower biases. These criteria select 2.2 million events in our off-resonance signal sample and 11.8 million events in our on-resonance calibration sample. About 27% of the events in the latter sample are $\Upsilon(4S)$ decays.

We evaluate the performance of the event selection using the data and a number of simulations, each consisting of a generator for a certain type of event combined with a detailed simulation of the *BABAR* detector using the GEANT4 [27] package. For signal $e^+e^- \rightarrow q\bar{q}$ events, we use the JETSET [8] event generator and obtain simulated selection efficiencies of 0.68 for $u\bar{u}$, $d\bar{d}$ and $s\bar{s}$ events, and 0.73 for $c\bar{c}$ events. As cross-checks, we also use the UCLA model combined with GEANT4, and the JETSET, UCLA and HERWIG models with a fast detector simulation and several different parameter sets. These give efficiency variations of at most 0.5%. In all cases, the largest signal loss is due to the requirement on θ^*_{thrust}, which ensures that the event is well contained within the sensitive volume of the detector, resulting in low p^* and multiplicity biases. We find consistency between data and simulation in a number of distributions of event and track quantities; the largest discrepancy we observe is a possible shift in the E_{tot} distribution (see Fig. 1), which could indicate an efficiency difference of at most 0.5%.

We use the KORALB [28] generator to simulate μ- and τ-pair events. The former provide a negligible contribution, but the latter are the largest source of background, estimated to be 4.5% of the selected events and to contribute up to 25% of the charged tracks at the highest

momenta. However, the relevant properties of τ-pair events are well measured [29], and their contributions can be simulated and subtracted reliably.

Radiative Bhabha events ($e^+e^- \rightarrow e^+e^-\gamma$) are an especially problematic background, as their cross section in the very forward and backward regions is larger than the $q\bar{q}$ cross section and varies rapidly with $\cos\theta^*$. Bremsstrahlung, photon conversions, and other interactions in the detector material are difficult to simulate in these regions, and can result in events with 3–6 tracks, most of which are from electrons or positrons. Simulations using the BHWIDE [30] generator predict that these events are reduced to a negligible level by criteria 1–5 plus a requirement that the highest-p_{lab} track in the 3- and 4-track events not be identified as an electron. However, a comparison of e^+ and e^- angular distributions in the selected data indicates a larger contribution. Therefore, we impose the tighter $e^{\pm}$ vetoes given in criterion 6, and estimate from the data a residual radiative Bhabha event contribution of 0.1% of the selected events and up to 8% of the charged tracks at our highest momenta and $|\cos\theta_{\text{lab}}|$ values.

Initial-state radiation (ISR), $e^+e^- \rightarrow \gamma e^+e^- \rightarrow \gamma q\bar{q}$, produces hadronic events with a lower effective CM energy. Low-energy ISR photons are present in all events and are simulated adequately in the JETSET model. The event selection is designed to suppress events with higher-energy ISR photons, including radiative return to the $\Upsilon(1S)$, $\Upsilon(2S)$ and $\Upsilon(3S)$ resonances (whose decays have very different inclusive properties from $e^+e^- \rightarrow q\bar{q}$ events) and events with a very energetic ISR photon recoiling against a hadronic system, which can mimic 2-jet events. Using the AFKQED generator [31], we find that the combination of the requirements on E_{tot} and θ^*_{thrust} reduces the energetic-ISR background to negligible levels, and the $\Upsilon(nS)$ background to one event in 10^5.

We use the GAMGAM [32] generator to study backgrounds from two-photon ($\gamma\gamma$) processes, $e^+e^- \rightarrow e^+e^-\gamma\gamma \rightarrow e^+e^- + \text{hadrons}$. Neither the total cross section nor those for any specific final states are known, but such events have relatively low track multiplicity and E_{tot} since the final-state $e^{\pm}$ and some of the hadrons generally go undetected along the beam direction. The E_{tot} distribution for events in the data satisfying all other selection criteria is shown in Fig. 1. It features a structure in the 1–5 GeV range that is not described by the signal plus τ-pair simulations, but can be described qualitatively by the addition of $\gamma\gamma$ events. Since the mixture of final states is unknown, we consider $\gamma\gamma \rightarrow \pi^+\pi^-\pi^+\pi^-$, which has the largest fraction of events with $E_{\text{tot}} > 5$ GeV of any final state with at least three tracks. The simulated E_{tot} distribution is shown as the shaded histogram in Fig. 1. If normalized to account for the entire excess in the data, such events would make up less than 1% of the selected sample ($5 < E_{\text{tot}} < 14$ GeV), with a track momentum distribution similar to that in τ-pair events. We take this as an upper
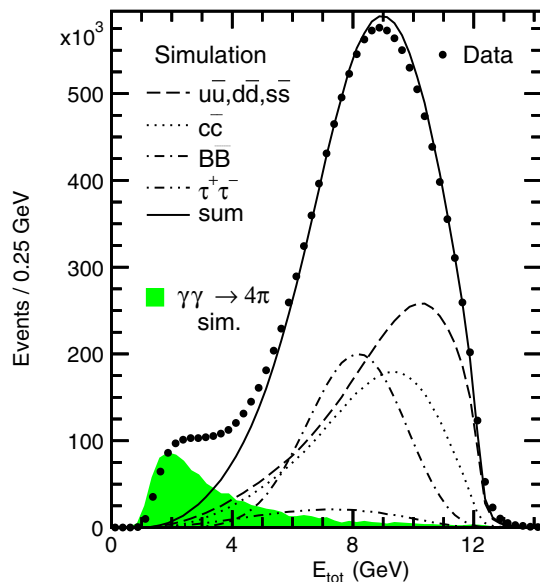

FIG. 1 (color online).   Distributions of the total visible energy per event, after all other selection criteria have been applied, in the on-resonance data and simulation. The sum of the hadronic and τ-pair simulations is normalized to the data in the region above 5 GeV, and the $\gamma\gamma$ simulation is normalized arbitrarily.

limit on our $\gamma\gamma$ background and vary its contribution over a wide range in evaluating the systematic uncertainty, as discussed in Sec. V B.

Backgrounds from beam-gas and beam-wall interactions can be studied using distributions of event vertex position in the data. From the distribution in distance from the beam axis for events satisfying all selection criteria except those on the vertex position, we conclude that the beam-wall background is negligible. From the distribution in z after including the requirement that the vertex be within 5 mm of the beam axis, we estimate that four beam-gas events are selected per 10^5 signal events. We neglect both of these backgrounds.

We consider a number of other possible backgrounds, including two-photon events with one or both $e^\pm$ detected and other higher-order quantum electrodynamics (QED) processes producing four charged leptons or two leptons and a $q\bar{q}$ pair; all are found to be negligible. We estimate that the selected sample is $95.4 \pm 1.1\%$ pure in $e^+e^- \to q\bar{q}$ events, with the background dominated by τ-pairs and the uncertainty by $\gamma\gamma$ events. The on-resonance calibration sample contains the same mixture of $e^+e^- \to q\bar{q}$ and background events, plus a 27% contribution from $\Upsilon(4S)$ decays.

IV. CHARGED TRACK SELECTION AND IDENTIFICATION

The identification of charged tracks as pions, kaons or protons is performed using an algorithm that combines the momentum and ionization energy loss measured in the DCH and the velocity measured via the Cherenkov angle in the DIRC. To ensure reliable measurements of these quantities, we require tracks to have (i) at least 20 measured coordinates in the DCH; (ii) at least 5 coordinates in the SVT, including at least 3 in z; (iii) a distance of closest approach to the beam axis of less than 1 mm; (iv) a transverse momentum $p_t > 0.2$ GeV/c; (v) a polar angle $\theta_{\rm lab}$ satisfying $-0.78 < \cos\theta_{\rm lab} < 0.88$; and (vi) an extrapolated trajectory that intersects a DIRC bar. The first criterion ensures good dE/dx resolution, the first three criteria select tracks from particles that originate from the primary interaction and do not decay in flight or interact before reaching the DIRC, and the combination of all six criteria yields tracks well within the DIRC fiducial volume, with good momentum and polar angle resolution.

These criteria suppress tracks from decays of long-lived particles such as K_S^0 and Λ hadrons, which are included in many previous measurements. Here, we report cross sections for two classes of tracks, denoted "prompt" and "conventional." We first measure prompt hadrons, defined as primary hadrons or products of a decay chain in which all particles have lifetimes shorter than 10^{-11} s. This includes products of all charmed hadron decays, as well as those of strongly or electromagnetically decaying strange particles, but not those of weakly decaying strange particles. We then obtain the conventional quantities by adding the decay daughters of particles with lifetimes in the range $1–3 \times 10^{-11}$ s, i.e., K_S^0 and weakly decaying strange baryons. For this we use existing measurements of K_S^0 and strange baryon production [33]. Either or both cross sections can be compared with other measurements, and used to test QCD and model predictions.

In selected simulated events, these criteria accept 82% of the prompt charged particles generated within the target $\theta_{\rm lab}$ range and with $p_t > 0.2$ GeV/c. This efficiency rises slowly from 80% at $p_{\rm lab} = 0.2$ GeV/c to 86% at the highest momentum, and is almost independent of particle type, polar angle, event flavor, and track multiplicity. Corrections to the simulation are discussed in Sec. V C.

Since the e^+e^- system is boosted in the laboratory frame, we divide the selected tracks into six regions of $\cos\theta_{\rm lab}$: $[-0.78, -0.33]$, $[-0.33, 0.05]$, $[0.05, 0.36]$, $[0.36, 0.6]$, $[0.6, 0.77]$ and $[0.77, 0.88]$, denoted $\theta 1$ to $\theta 6$, and analyze each region separately. These correspond to regions of roughly equal width in $\cos\theta^*$ between -0.92 and $+0.69$. The tracks in each region arise from the same underlying p^* distribution, but are boosted into different ranges of $p_{\rm lab}$. Also, heavier particles are boosted to higher $\cos\theta_{\rm lab}$, with low-p^* protons and kaons populating the forward $\cos\theta_{\rm lab}$ regions preferentially. Thus we perform multiple (up to six) measurements for each p^* value, each from a different $p_{\rm lab}$ range and in a different region of the detector. Their comparison provides a powerful set of cross-checks on detector performance and material interactions, backgrounds, the true θ^* and p^* distributions, and the boost value itself.

A. Charged hadron identification

The dE/dx measurement from the DCH provides very good separation between low-$p_{\rm lab}$ particles, i.e., between $K^\pm$ and $\pi^\pm$ ($p/\bar{p}$ and $K^\pm$) below about 0.5(0.8) GeV/c. There is also modest separation, of 1–3 standard deviations (σ), in the relativistic rise region above about 2 GeV/c, and the separation varies rapidly at intermediate $p_{\rm lab}$. For each accepted track, we calculate a set of five likelihoods $L_i^{\rm DCH}$, $i = e, \mu, \pi, K, p$, each reflecting the degree of consistency of its measured dE/dx value with hypothesis i.

The Cherenkov angle measurement from the DIRC provides very good separation between particles with $p_{\rm lab}$ between the Cherenkov threshold and the resolution limit of about 4 GeV/c for $\pi^\pm$ vs $K^\pm$ and 6.5 GeV/c for $K^\pm$ vs $p/\bar{p}$. The number of expected photons varies rapidly with $p_{\rm lab}$ just above threshold, and the number detected for each track provides additional information. A track can be classified as being below threshold by counting the detected photons at the angles expected for each above-threshold particle type and comparing with the hypothesis that only background is present. To make full use of this information, we maximize a global likelihood for the set of

reconstructed tracks in each event, which considers backgrounds, photons that could have been emitted by more than one track, and multiple angles from a given track. For each track, we calculate a set of five likelihoods L_i^{DIRC}, $i = e, \mu, \pi, K, p$, assuming the best hypothesis for all other tracks. These provide $K^\pm$-$\pi^\pm$ ($p/\bar{p}$-$K^\pm$) separation that rises rapidly with p_{lab} from zero at the $\pi^\pm$ ($K^\pm$) Cherenkov threshold of $0.13(0.48)$ GeV/c, to a roughly constant value, from which it falls off above about $2.5(4.5)$ GeV/c.

To make use of both DCH and DIRC information, we consider the log-likelihood differences $l_{ij}^{\mathrm{det}} = \ln(L_i^{\mathrm{det}}) - \ln(L_j^{\mathrm{det}})$, where det = DCH, DIRC, and we identify tracks by their positions in the l_{ij}^{DCH} vs l_{ij}^{DIRC} planes. The procedure is illustrated in Fig. 2 for simulated $\pi^\pm$ (lower left) and $K^\pm$ (upper right) with $0.6 < p_{\mathrm{lab}} < 0.625$ GeV/c and $\cos\theta_{\mathrm{lab}} > 0.05$. Here the DIRC provides clear separation for all but a few percent of the tracks (most of the entries at the left and right edges are overflows), but long tails are visible in the $l_{K\pi}^{\mathrm{DIRC}}$ distributions for both $\pi^\pm$ and $K^\pm$. The DCH separation is smaller, but the tails are shorter. To be identified as a $\pi^\pm$, a track must lie below a line in the $l_{K\pi}^{\mathrm{DCH}}$-$l_{K\pi}^{\mathrm{DIRC}}$ plane (see Fig. 2) and below another line in the $l_{p\pi}^{\mathrm{DCH}}$-$l_{p\pi}^{\mathrm{DIRC}}$ plane. Similarly, an identified $K^\pm$ lies above a line (dashed in Fig. 2) in the $l_{K\pi}^{\mathrm{DCH}}$-$l_{K\pi}^{\mathrm{DIRC}}$ plane and below a line in the l_{pK}^{DCH}-l_{pK}^{DIRC} plane, and an identified $p/\bar{p}$ lies above lines in the $l_{p\pi}^{\mathrm{DCH}}$-$l_{p\pi}^{\mathrm{DIRC}}$ and l_{pK}^{DCH}-l_{pK}^{DIRC} planes.

The parameters describing the lines vary smoothly with p_{lab} and θ_{lab}, and are optimized [34] to keep the misidentification rates as low as reasonably possible, while maintaining high identification efficiencies that vary
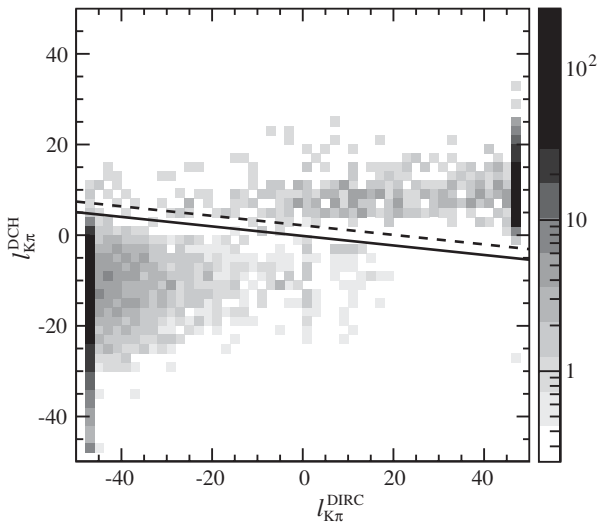

FIG. 2. Simulated distribution of the K-π log-likelihood difference $l_{K\pi}$ from the DCH vs that from the DIRC for $\pi^\pm$ and $K^\pm$ in hadronic events generated with $0.6 < p_{\mathrm{lab}} < 0.625$ GeV/c and $\cos\theta_{\mathrm{lab}} > 0.05$. The $\pi^\pm$ and $K^\pm$ are concentrated in the lower left and upper right regions, respectively. The edge bins include overflows. The solid (dashed) line represents an upper (lower) bound on identified $\pi^\pm$ ($K^\pm$).

slowly with p_{lab} and $\cos\theta_{\mathrm{lab}}$. The slopes are zero (i.e. only dE/dx information is used) for p_{lab} below the lower of the two Cherenkov thresholds, begin to decrease slowly at that threshold, and become large and negative above about 2.5 GeV/c; although dE/dx provides some separation in this region, the systematic uncertainties are minimized by using it only to reject outlying tracks. In some cases the two lines in a given plane are the same; in most cases they are nearly parallel and separated by a few units, and tracks in between are not identified as any hadron type. Fewer than 0.1% of the tracks are identified as more than one type, and these are reclassified as unidentified.

Electrons and muons represent only a small fraction of the tracks in hadronic events at $E_{\mathrm{CM}} \approx 10$ GeV (at most 2%), and their production is understood at the level of 10% or better (see Sec. V E). They can be suppressed at this point using calorimeter and muon system information, and we have done this as a cross-check, obtaining consistent results. However, this also rejects some signal tracks, and the total systematic uncertainties are minimized by including $e^\pm$ and $\mu^\pm$ in the pion category at this stage, and subtracting them later. We therefore define a $(e\mu\pi)^\pm$ sample. High-momentum $e^\pm$ and almost all $\mu^\pm$ are indistinguishable from $\pi^\pm$ in the DCH or DIRC, so are included by the criteria noted so far. The DIRC does separate $\mu^\pm$ from $\pi^\pm$ in a narrow p_{lab} range near 0.2 GeV/c, but we use only dE/dx information in this range. To accommodate low-momentum $e^\pm$, we include tracks with p_{lab} below 2 GeV/c that satisfy requirements in the $l_{e\pi}^{\mathrm{DCH}}$-$l_{e\pi}^{\mathrm{DIRC}}$ and l_{eK}^{DCH}-l_{eK}^{DIRC} planes.

We quantify the performance of our hadron identification procedure in terms of a momentum-dependent identification efficiency matrix $\boldsymbol{E}$, where each element E_{ij} represents the probability that a selected track from a true i-hadron is identified as a j-hadron, with $i, j = (e\mu\pi)$, K, p. The matrix predicted by the detector simulation for our most forward polar angle region, $\theta 6$, which covers the widest p_{lab} range, is shown as the dashed lines in Fig. 3. The efficiencies for correct identification are predicted to be very high at low p_{lab}, where dE/dx separation is good, then transition smoothly to a plateau where the Cherenkov angle provides good separation, and then fall off at higher p_{lab} where the Cherenkov angles for different particles converge. The predicted probabilities for misidentifying a particle as a different type are below 2.5%. Essentially all tracks are identified as some particle type at low p_{lab}, 1%–3% are classified as ambiguous in the plateau regions, and larger fractions are so classified as the efficiency falls off, since we choose to maintain constant or falling misidentification rates.

Similar performance is predicted in the other $\cos\theta_{\mathrm{lab}}$ regions. In $\theta 1$ and $\theta 2$, the two most backward regions, p_{lab} does not exceed 3.5–4 GeV/c, so no falloff is visible in E_{pp} at high p_{lab}, and $E_{\pi\pi}$ and E_{KK} drop only to 30%–70%
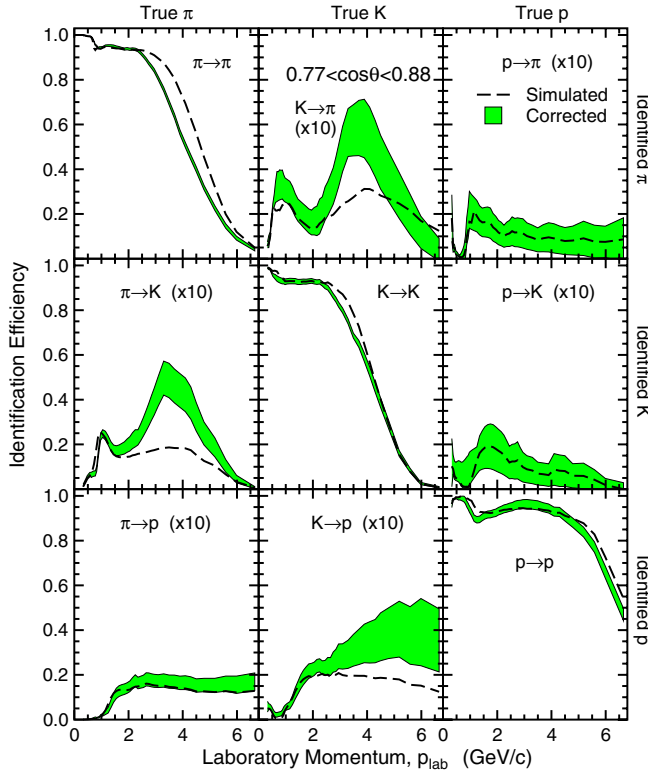
FIG. 3 (color online). The simulated (dashed lines) and corrected (gray/green bands) efficiency matrix for the most forward polar angle region, $\theta 6$, where $0.77 < \cos\theta_{\mathrm{lab}} < 0.88$. The widths of the bands indicate the uncertainties derived from the control samples discussed in the text. The off-diagonal elements have been scaled up by a factor of 10 for clarity.

of their plateau values. Thus we are able to measure the high p^* range well in multiple $\cos\theta_{\mathrm{lab}}$ regions. In the next few subsections, however, we focus on $\theta 6$, since it spans the widest range in efficiencies and requires the largest corrections to the simulation.

B. Calibration of the identification efficiencies

We calibrate the efficiency matrix from the combined off- and on-resonance data set, using samples of tracks with known hadron content and characteristics as similar as possible to our selected tracks. For example, we construct $K_S^0 \rightarrow \pi^+ \pi^-$ candidates from tracks satisfying criteria (i) and (iv)–(vi) presented at the beginning of Sec. IV, with a less restrictive requirement of three coordinates in the SVT and an additional requirement that there be a coordinate from one of the two outer layers of the DCH. Pairs of oppositely charged tracks must have a fitted vertex more than 0.5 cm from the beam axis, a reconstructed total momentum direction within 50 mrad of the line between their fitted vertex and the event vertex, and an invariant mass in the range 486–506 MeV/c^2. The percent-level non-K_S^0 contribution is predominantly from pions, so these tracks constitute a clean sample of $\pi^\pm$ that are produced in hadronic events and cross most of the tracking system.

In simulated events, this sample has $E_{\pi j}$ values within 0.5% of those of the prompt $\pi^\pm$ in the same events. We calculate efficiencies from this K_S^0 sample in both data and simulation, and use their differences to correct the prompt $\pi^\pm$ simulation. This sample covers p_{lab} up to about 1.5 GeV/c with high precision.

A similar selection of $\Lambda \rightarrow p\pi^-$ and $\bar{\Lambda} \rightarrow \bar{p}\pi^+$ candidates provides a sample of 0.4–3.5 GeV/c $p/\bar{p}$ (and another sample of soft pions) in hadronic events. We also reconstruct two samples of $\phi \rightarrow K^+ K^-$ decays in which either the K^+ or K^- is identified, providing 0.2–2 GeV/c K^- and K^+ samples that are subsamples of our main sample. These samples contain substantial backgrounds, and we extract E_{pj}, $E_{\bar{p}j}$, E_{K^+j} and E_{K^-j} from sets of simultaneous fits to the four $p/\bar{p}\pi^\mp$ or K^+K^- invariant mass distributions in which the $p/\bar{p}$ or the other kaon is identified as a pion, kaon, proton or no type.

We obtain samples of 0.6–5 GeV/c $\pi^\pm$ and $K^\pm$ by reconstructing candidate $D^{\star+} \rightarrow D^0\pi^+ \rightarrow K^-\pi^+\pi^+$ (and charge conjugate) decays and selecting those with a $K^-\pi^+\pi^+ - K^-\pi^+$ mass difference in the range 143–148 MeV/c^2. The $K^-\pi^+$ invariant distribution shows a D^0 signal with a peak signal-to-background of 11. These tracks are predominantly from $\Upsilon(4S)$ decays and $c\bar{c}$ events, but have simulated E_{Kj} and $E_{\pi j}$ values within 1% and 0.5%, respectively, of those from all prompt $K^\pm$ and $\pi^\pm$ in hadronic events. Requiring the π^- (K^+) candidate track to be so identified and the K^- (π^+) track to satisfy our selection criteria, we evaluate E_{K^-j} (E_{π^+j}) as the fraction of the sideband-subtracted entries in the D^0 peak in which the K^- (π^+) is identified as type j.

We select $e^+e^- \rightarrow \tau^+\tau^-$ events in which one of the τ decays contains a single charged track (1-prong) and the other contains one or three (3-prong) charged tracks. These tracks constitute $(e\mu\pi)^\pm$ samples that are not from a hadronic jet environment and have different $e^\pm{:}\mu^\pm{:}\pi^\pm$ content, as well as a small but well known $K^\pm$ component. However, these samples have simulated identification efficiencies within a few percent of those for $\pi^\pm$ in hadronic events, and they allow us to study high-p_{lab} tracks and tracks that are isolated (1-prong) or relatively close together (3-prong) in the detector. We also apply independent electron and muon selectors to the 1-prong sample, in order to check that the small differences in performance between $e^\pm$, $\mu^\pm$ and $\pi^\pm$ are simulated correctly.

Results from the different calibration samples are consistent where they overlap, as are those from positively and negatively charged tracks and from on- and off-resonance data. Considering the set of constraints provided by these samples, we derive corrections to the simulated E_{ij} elements that vary smoothly with p_{lab} and $\cos\theta_{\mathrm{lab}}$. The correction to each E_{ij} in each $\cos\theta_{\mathrm{lab}}$ region is a continuous, piecewise-linear function of p_{lab}, with an uncertainty given by the statistically most precise calibration sample at each point. The resulting calibrated efficiencies in the $\theta 6$

region are shown as the gray/green bands in Fig. 3; their centers represent the calibrated efficiencies, and their half-widths the uncertainties.

The pion efficiencies $E_{\pi j}$ (left column of Fig. 3) are measured well over the full p_{lab} range, with corrections and uncertainties near or below the percent level for $p_{\mathrm{lab}} <$ 2.5 GeV/c. There are substantial corrections to $E_{\pi\pi}$ and $E_{\pi K}$ in the 3–5 GeV/c range, which is sensitive to the details of the DIRC geometry and backgrounds.

The kaon efficiencies E_{Kj} (middle column of Fig. 3) are measured for $p_{\mathrm{lab}} > 0.4$ GeV/c with somewhat larger uncertainties than for $E_{\pi j}$. The corrections to E_{KK} and $E_{K\pi}$ are similar at most p_{lab} to those on $E_{\pi\pi}$ and $E_{\pi K}$, respectively, as expected from the near symmetry in the dE/dx and Cherenkov angle measurements. They have opposite sign, as expected, in the region just above kaon threshold, 0.5–1 GeV/c. The large correction to E_{Kp} near 6 GeV/c is consistent with the corrections to $E_{\pi K}$ and $E_{K\pi}$ with p_{lab} scaled by a factor of roughly 1.9, the ratio of the proton and kaon masses, as expected.

Below 0.4 GeV/c, the kaon calibration samples have high backgrounds and do not yield useful results. However, the identification efficiencies are very high, we expect strong correlations between hadron types up to 0.6 GeV/c, and the calibration data are consistent with full correlation between 0.4 and 0.6 GeV/c. Therefore, we apply the same small corrections to E_{KK} as for $E_{\pi\pi}$, and to $E_{K\pi}$ and E_{Kp} as for $E_{\pi K}$ at 0.2 GeV/c, with the uncertainty doubled arbitrarily to account for any incomplete correlation. We apply the corrections and uncertainties from the kaon calibration samples to E_{KK} and $E_{K\pi}$ at 0.6 GeV/c, and vary the corrections and uncertainties linearly between 0.2 and 0.6 GeV/c. Due to the higher proton mass, the corresponding region in E_{Kp} extends to 1.0 GeV/c, so we match the corrections at that value.

The proton efficiencies E_{pj} (right column of Fig. 3) are measured well in the range 0.8–3.5 GeV/c, and the corrections show the expected correlations with the other elements. Again, we expect complete correlations at low p_{lab}, and we apply the same corrections to $E_{p\pi}$, E_{pK}, and E_{pp} as for $E_{\pi p}$, E_{Kp}, and E_{KK}, respectively, at 0.2 GeV/c, with doubled uncertainties. We then match them to their respective proton calibration values at 1 GeV/c. Above 3.5 GeV/c, the statistical precision of the proton calibration sample is limited, and we exploit the correlation expected between E_{pp} in the 2–6.5 GeV/c range, and $E_{\pi\pi}$ and E_{KK} in the corresponding 1.1–3.4 GeV/c range. The three corrections are consistent in the lower part of this range, and in the upper part we average the corrections to $E_{\pi\pi}$ and E_{KK}, scale them up in p_{lab}, and apply them to E_{pp} with an uncertainty twice that on the E_{KK} correction. We match to the proton calibration sample at 3.1 GeV/c, where the uncertainties from the two approaches are comparable.

Due to the low value of the proton fraction, the criteria for proton identification are more stringent than for pion or

kaon identification at high p_{lab}, so that $E_{p\pi}$ and E_{pK} are smaller than the other misidentification rates, as are the corrections.

Corrections to the efficiencies in the other $\cos\theta_{\mathrm{lab}}$ regions are similar in form and generally smaller than those shown in Fig. 3. Even though the uncertainties of some misidentification rates are relatively large, they result in small systematic uncertainties of the result, since the rates themselves are sufficiently low. The uncertainties of the correct identification efficiencies are important, especially at high p_{lab}. However, high-p^* particles are measured well in the more backward $\cos\theta_{\mathrm{lab}}$ regions, and the final result is an average over the six regions.

V. MEASUREMENT OF THE DIFFERENTIAL CROSS SECTIONS

The objects of this measurement are the production cross sections per unit p^*, $(1/\sigma_{\mathrm{tot}}^{\mathrm{had}})(d\sigma_i/dp^*)$, $i = \pi$, K, p, normalized to the total hadronic event cross section $\sigma_{\mathrm{tot}}^{\mathrm{had}} = 3.39$ nb at our CM energy of 10.54 GeV. We present these in the equivalent and conventional form $(1/N_{\mathrm{evt}})(dn_i/dp^*)$, where N_{evt} and n_i are the numbers of hadronic events and i-particles, respectively.

From our samples of identified $\pi^{\pm}$, $K^{\pm}$ and $p/\bar{p}$, we use the corrected identification efficiency matrices described in the preceding section to construct the raw production rates $(1/N_{\mathrm{evt}}^{\mathrm{sel}})(dn_i/dp_{\mathrm{lab}})$, $i = (e\mu\pi)$, K, p, defined as the numbers of reconstructed particles per selected event per unit momentum in the laboratory frame. We subtract backgrounds and apply corrections to account for the effects of detector efficiency and resolution, and the event selection procedure. We do this separately in each of the six $\cos\theta_{\mathrm{lab}}$ regions, and also in the on-resonance sample for control purposes.

We transform each corrected rate into a cross section in the e^+e^- CM frame, where we compare and combine the results from the six $\cos\theta_{\mathrm{lab}}$ regions. Subtracting the expected contributions from leptons, we obtain our prompt results, $(1/N_{\mathrm{evt}})(dn_i^{\mathrm{prompt}}/dp^*)$. We add the expected contributions from decays of K_S^0 and weakly decaying strange baryons to obtain conventional cross sections, and we calculate ratios of cross sections and charged hadron fractions. Each of these steps is described in detail in the following subsections, and each involves a number of systematic checks and uncertainties. The systematic uncertainties are summarized in the final subsection.

A. Cross sections in the laboratory frame

In each p_{lab} bin, we count n_j, the number of tracks identified as type $j = (e\mu\pi)$, K, p. These can be related to the true fractions f_i of tracks that are of type i by $n_j = n\Sigma_i E_{ij}f_i$, where n is the total number of selected tracks and the efficiency matrix $\boldsymbol{E}$ is described in Sec. IV. We first solve this set of equations in each bin for the three f_i

values, and check that their sum is consistent with unity. This check is sensitive to many systematic effects on E, and if we apply no corrections to the simulated E, we find significant differences from unity in several places, most notably in the DCH-DIRC crossover region near 0.7 GeV/c and at the highest momenta in the forward polar angle regions. The on-resonance control sample shows the same differences. After the corrections, the sum is consistent with unity in all bins within the systematic uncertainties obtained by propagating the uncertainties on the nine E_{ij}. The fractions and their sum in the most forward $\cos\theta_{lab}$ region, $\theta6$, are shown in Fig. 4. Neighboring points are correlated due to the efficiency correction procedure.

We then recalculate the fractions with the added constraint that their sum be unity. The recalculated fractions are also shown in Fig. 4, and are almost indistinguishable from the unconstrained fractions. In the systematic error propagation, we account for the constraint by varying the three efficiencies E_{jj} independently, and in each case varying both corresponding misidentification rates E_{jk} in the opposite direction. Both the statistical and systematic uncertainties decrease slightly with the addition of the constraint. It also introduces strong statistical correlations
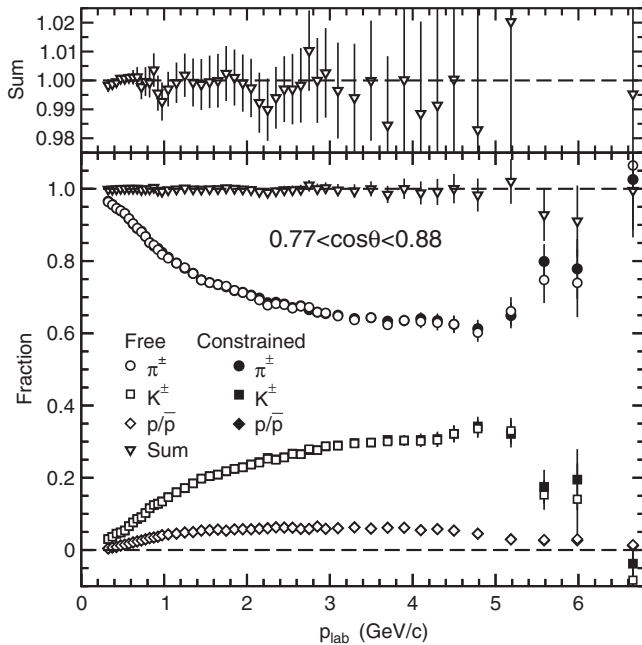
between the three particle types, but since the results are dominated by systematic effects, we neglect these.

Several additional systematic checks are performed, including varying the misidentification rates by three times their uncertainties, changing the p_{lab} ranges over which we fit the corrections to E, using different event flavor mixtures in the simulation, and using the efficiencies measured in the control samples directly, rather than using them to correct the simulation. We find no change in the results larger than the relevant systematic uncertainty.

Each fraction is multiplied by the number of accepted tracks in that bin and divided by the number of selected hadronic events and by the bin width to obtain raw normalized cross sections.

B. Background subtraction

We subtract backgrounds due to other physics processes, interactions in the detector material, and strange-particle decay products. As discussed in Sec. III, there are three physics processes with non-negligible background contributions to our event sample: τ-pair, two-photon and radiative Bhabha events. Figure 5 shows the simulated fractional contributions to the selected tracks in region $\theta6$ from these three sources.

The contribution from τ-pair events is small at low p_{lab}, but grows steadily to over 20% at higher momenta. There are similar contributions in the other $\cos\theta_{lab}$ regions. The simulation of τ-pair production and decay is reliable at the subpercent level, and our detector simulation is reliable (after the corrections described in Sec. V C) to 1%–2%. However, since we normalize per selected event, we must consider the relative event selection efficiency. Here, our simulation is also quite reliable for τ-pairs, but less so for hadronic events, discussed in Sec. V F, and the uncertainty corresponds to a roughly constant 10% relative uncertainty
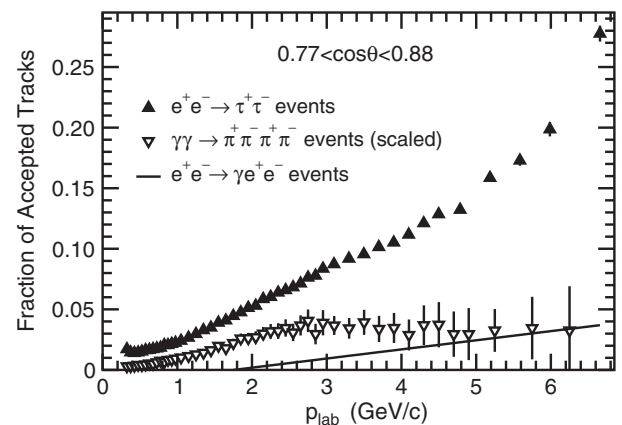

FIG. 4. Raw $\pi^{\pm}$ (circles), $K^{\pm}$ (squares) and $p/\bar{p}$ (diamonds) fractions measured in $\theta6$, the most forward $\cos\theta_{lab}$ region. The solid (open) symbols represent the results with (without) the constraint that they sum to unity in each p_{lab} bin. They are indistinguishable in most cases. The sums of unconstrained fractions are shown as the triangles, and in an expanded view in the upper plot. The error bars include statistics and the systematic uncertainties arising from the calibration of the particle identification efficiencies.

FIG. 5. Fractional contributions to the selected track sample from τ-pair (up triangles), $\gamma\gamma \to 2\pi^{+}2\pi^{-}$ (down triangles) and radiative Bhabha (line) events in $\theta6$, as functions of the measured p_{lab}. The $\gamma\gamma \to 2\pi^{+}2\pi^{-}$ cross section is scaled as discussed in the text, and represents an upper bound.

on the tracks from τ-pair events. We therefore subtract the absolute prediction of the simulation with a 10% relative uncertainty.

The contribution from two-photon events is not well understood, but we can set an upper limit by scaling our simulated $\gamma\gamma \rightarrow 2\pi^+2\pi^-$ sample to account for the structure observed at low E_{tot}, discussed in Sec. III and shown in Fig. 1. The resulting contribution is shown by the triangles in Fig. 5. Due to the kinematics of $\gamma\gamma$ events and the detector acceptance, this background is highest in $\theta6$, somewhat smaller in $\theta1$, and about half as large in the central regions. Most $\gamma\gamma$ events contain more charged and neutral hadrons than the $2\pi^+2\pi^-$ final state, some of which are outside the acceptance, yielding smaller values of E_{tot}. Therefore, we expect to select far fewer events than indicated by this sample, containing mostly lower-p_{lab} tracks, and Fig. 5 shows a substantial overestimate at high p_{lab} and an upper bound at lower p_{lab}. This limit is at most 4% and well below the τ-pair contribution, so we make no correction, but assign a systematic uncertainty corresponding to one half of the limit in each bin.

As discussed in Sec. III, the simulation predicts a negligible contribution from radiative Bhabha events, but may be unreliable, especially in the forward and backward directions. Due to the t-channel contribution to their production process, such events would exhibit a charge asymmetry with a characteristic dependence on p_{lab} and $\cos\theta_{lab}$. In our selected $(e\mu\pi)^{\pm}$ sample, we observe significant differences between positively and negatively charged tracks that reach 10% and -4% at the highest p_{lab} in the most backward and forward $\cos\theta_{lab}$ regions, respectively, and show an angular dependence consistent with radiative Bhabha events. We make a smooth parametrization of this difference, and subtract it from our $(e\mu\pi)$ cross section. The effect is a few percent at high momenta in the forward (see Fig. 5) and backward $\cos\theta_{lab}$ regions, but below 1% in the central regions. This procedure also accounts for any residual events from $e^+e^- \rightarrow e^+e^-e^+e^-$ or other higher-order QED processes with forward-peaking cross sections.

After subtracting these τ-pair and radiative Bhabha backgrounds, we normalize by the estimated number of hadronic events in the selected sample, to obtain background-subtracted differential cross sections.

Interactions of particles with the detector material can lead to tracking inefficiencies, which are discussed in Sec. V C, and also to the production of extraneous charged tracks that satisfy the signal-track criteria. Most interaction products fail the selection criteria, but two categories require care: a highly asymmetric photon conversion can produce an electron or positron that points back to the event vertex; and a pion interacting with a nucleon through a Δ resonance can produce a proton nearly collinear with the pion. Figure 6 shows the simulated fractional contributions from interaction products. Photon conversions account for the vast majority, as much as 1.5% of the
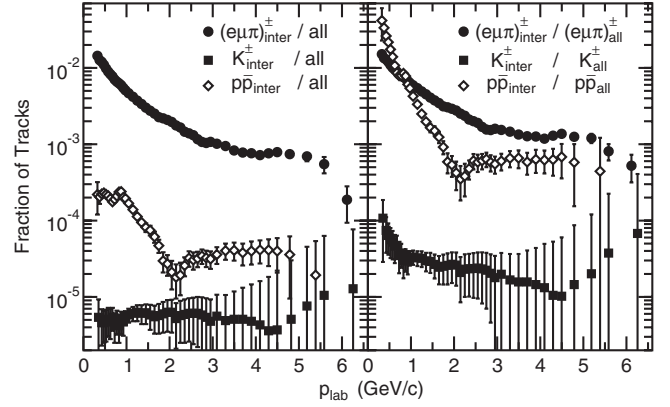

FIG. 6. Simulated fractional contributions to the overall selected track sample (left) and the selected tracks of the same type (right) from pions (circles), kaons (squares) and protons (diamonds) produced through interactions in the detector material. Results for tracks in the on-resonance sample in $\theta6$ are shown, and the point-to-point variations have been smoothed.

selected tracks at the lowest p_{lab} value, but well below 1% over most of the p_{lab} range. We have measured the photon conversion rate in our data, and the simulated rate lies within 20% of this rate for all p_{lab}, so we subtract the simulated fractional contribution to the $(e\mu\pi)$ sample, shown in the right plot of Fig. 6. Since the measurement uses conversions with two tracks that fail our selection criteria, and the chance of passing depends on details of the detector simulation, we assign an arbitrary and conservative systematic uncertainty equal to 50% of the correction.

Protons produced in the detector material represent a small fraction of all selected tracks, but as much as 4% and 15% of those identified as protons in the lowest kinematically allowed p_{lab} bins in $\theta6$ (shown in Fig. 6) and $\theta1$, respectively. There is a concentration of material in the *BABAR* detector between the SVT and the DCH, and protons produced in this region can be studied using tracks that are identified by our algorithm as protons, but have measured dE/dx in the SVT inconsistent with a proton and consistent with a pion. Our study revealed a problem with the simulation of the Δ resonances in our version of GEANT, for which we apply a correction. We subtract the corrected simulated contributions of such protons and apply a uniform 50% relative uncertainty, which is slightly larger than the statistical uncertainty on the study in each $\cos\theta_{lab}$ region.

Very few antiprotons are produced in material interactions, but they suffer from similar uncertainties in the loss rate (see Sec. V C). We measure p and $\bar{p}$ cross sections separately, and the results are consistent within these systematic uncertainties. The simulation predicts a very small number of kaons from detector interactions, and we subtract the predicted fraction with an arbitrary 50% uncertainty. The simulation also includes tracks arising

from beam-related backgrounds and noise in the detector, by overlaying untriggered events from beam crossings close in time to triggered events. These are a small fraction of the tracks in Fig. 6, and are included in the correction.

There are also residual tracks in the sample from weak decays of strange particles that we must exclude from our prompt sample. We evaluate these by reweighting our simulated K_S^0 and K_L^0 spectra to reproduce the average of the measured K_S^0 spectra at or near our CM energy [33], reweighting our simulated Λ spectrum to match the measured spectrum [33], and applying the same weights to our simulated Σ baryon spectra. The weighted simulation predicts that at the lowest p_{lab}, about 2% of the selected $(e\mu\pi)^{\pm}$ tracks are from K_S^0 decays and a further 3% from strange baryon decays, with both contributions falling rapidly as p_{lab} increases. About 13% of the selected $p/\bar{p}$ tracks in the lower half of the p_{lab} range are from strange baryon decays, and this falls slowly toward 4% at the highest p_{lab}. There are also smaller contributions of $(e\mu\pi)^{\pm}$ from K_L^0, $K^{\pm}$ and $\pi^{\pm}$ decays, and $K^{\pm}$ from Ω^- decays.

We subtract the simulated fractions of these tracks from each cross section, and assign systematic uncertainties to the K_S^0 and strange baryon contributions based on the uncertainties on the corresponding measured spectra [33]. The assigned uncertainties are parametrized with smooth functions that vary with p^* between 5% and 35% over the bulk of distributions, and increase toward 100% at zero and the kinematic limits, where the contributions vanish. We assign an arbitrary 50% relative uncertainty to all other sources.

C. Track selection efficiency

Next, we correct the background-subtracted cross sections for the track and event selection efficiencies, to obtain corrected cross sections, per hadronic event, for each hadron type. Figure 7 shows these efficiencies for the three particle types as functions of p_{lab} in region $\theta 6$.

The solid lines in Fig. 7 represent the simulated fractions of particles within this $\cos\theta_{\mathrm{lab}}$ region that are in a selected event. They are well below unity here, since $\theta 6$ is near the edge of our acceptance, but peak near 95% in the central regions. Most of the p_{lab} dependence arises from the two-jet topology of $e^+e^- \to q\bar{q}$ events. Softer tracks are farther, on average, from the thrust axis, and their distribution becomes nearly isotropic at very low p_{lab}, where all three fractions approach the average event selection efficiency of 72%. The highest-p_{lab} tracks tend to define the thrust axis, and the fractions drop at high p_{lab} in $\theta 1$ and $\theta 6$, which span our thrust axis requirement. The track multiplicity and electron veto criteria introduce smaller biases against high-p_{lab} tracks in all $\cos\theta_{\mathrm{lab}}$ regions.

These biases depend on several aspects of the hadronization process, which is the object of this measurement. Since it is not understood in detail, especially in extreme
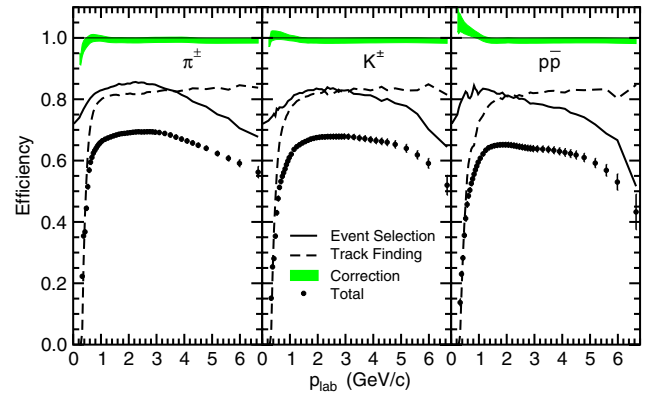

FIG. 7 (color online).   Efficiencies for charged pions (left), kaons (center) and protons (right) to produce a selected track in the most forward $\cos\theta_{\mathrm{lab}}$ region in the on-resonance sample. The solid (dashed) lines represent the simulated fractions of such particles that are in selected events (of those particles that produce a selected track), and the gray/green bands are the products of the corrections discussed in the text, with their half-widths representing the uncertainties. The points are the products of the three lines/bands.

cases such as events with one very high-momentum track, we compare a number of inclusive track momentum and polar angle distributions in the data and simulation. We find a number of inconsistencies, some of which are described in Sec. VI. We address these by reweighting the simulated distributions to match the data, and by comparing a number of different generators and parameter values without detector simulation. We find changes in the event selection bias that are much smaller than the other uncertainties.

The dashed lines in Fig. 7 represent the simulated efficiencies for a particle in a selected event to produce a selected track. They are zero by definition for tracks with p_t below 0.2 GeV/c. The $\pi^{\pm}$ efficiency rises rapidly to 80% at 1 GeV/c, then increases slowly to an asymptotic value of about 85%. The kaon and proton efficiencies rise more slowly due to decays in flight and interactions in the detector material, respectively, then show behavior similar to the pions. This strong similarity is present for prompt particles, but the pion and proton efficiencies would decrease by up to 10% if K_S^0 and strange baryon decay products were included. These efficiencies vary little with polar angle.

We perform a number of studies to check and correct the simulated efficiencies [35]. A study of high quality tracks reconstructed in the SVT alone and extrapolated into the DCH gives information on both the intrinsic efficiency of the DCH and losses in the material between them. The simulation is found to be consistent with the data at high p_{lab}, but corrections of up to 3% are needed at lower p_{lab}. A similar study uses pairs of DCH tracks that form a K_S^0 or Λ candidate with a reconstructed vertex inconsistent with the event vertex but within the innermost layer of the SVT.

This gives information on the SVT efficiency, indicating the need for 1%–3% corrections at low p_{lab} and 0.5% corrections overall. A further study [36] of identified tracks with a kink (which revealed the problem in GEANT4 noted in Sec. V B) provides a check of the simulation of decays in flight, and indicates different material interaction corrections for pions, kaons and protons.

We also compare the fraction of tracks in the data and simulation that satisfy each of the selection criteria after all combinations of the other criteria have been applied. An overall difference could arise from a deficiency in either the physics or the detector simulation, so is of limited use. However, by studying differences as a function of identified track type, charge and polar angle, a number of potential problems with the detector simulation can be corrected or limited. We find consistency overall, but we confirm the discrepancies found in the studies just described, and also identify a problem with the simulation of the DCH hit thresholds that affects particles with small dE/dx. The effect is small except at p_{lab} values near the minimum of the dE/dx curve in the most central $\cos\theta_{lab}$ region, where it is as large as 1.3%.

Combining this information, we derive a set of corrections to the simulated efficiencies. These are shown as bands in Fig. 7, where the half-widths indicate the total uncertainties. The corrections are below 1% with uncertainties of 0.8% for $p_{lab} > 1$ GeV/c. At lower momenta, the correction to the kaon efficiency is at the percent level, but the pion (proton) efficiency is reduced (increased) by as much as 6.5% (9%) with uncertainties of up to one third of the correction. The corrections have the same form in the other $\cos\theta_{lab}$ regions, but are smaller in proportion to the amount of material traversed.

The simulated interaction rates are different for positively and negatively charged particles, as are some of the corrections. We perform the analysis separately for the two charges up to this point, and compare their cross sections at each stage in each $\cos\theta_{lab}$ region. Without the efficiency correction, we observe differences consistent with expectations. The fully corrected cross sections are consistent with each other within the relevant systematic uncertainties.

D. Cross sections in the CM frame

At this point we have cross sections for hadrons produced in six $\cos\theta_{lab}$ regions as functions of their measured p_{lab}. The measured p_{lab} value can differ from the true value because of finite momentum resolution, and low-p_{lab} particles can suffer energy loss before the DCH that reduces the measured p_{lab}. These are both small effects on this measurement, and it is convenient to include corrections for them in the transformation to the CM frame, discussed in this section. We verify the quality of our simulation by comparing the masses and widths of the $K_S^0 \to \pi^+\pi^-$, $\phi \to K^+K^-$, $\Lambda \to p\pi^-$ and $\Lambda_c^+ \to pK^-\pi^+$ signals with

those measured in the data (see Ref. [37]). The small differences have negligible effects on this measurement, and we assign no systematic uncertainty from this source.

Differential cross sections in the laboratory frame can, in principle, be transformed into the CM frame in a model-independent way. However, large nonlinearities for low-p_{lab} and p^* particles make this challenging, and we choose instead a method that is explicitly model dependent, but allows us to check the simulation at each stage and evaluate systematic uncertainties reliably.

For each particle type and each $\cos\theta_{lab}$ region, we first calculate production fractions F_j and an inverse migration matrix $\mathbf{W}$ from the simulation, where F_j is the fraction of particles produced in the jth p^* bin that are boosted into this $\cos\theta_{lab}$ region, and W_{ij} is the fraction of those boosted into the ith p_{lab} bin that arise from the jth p^* bin. The transformation can then be written as

$$dn_j/dp^* = (1/F_j)\sum_i W_{ij}dn_i/dp_{lab}. \qquad (1)$$

The widths of the $\cos\theta_{lab}$ regions are such that 4–5 p_{lab} bins contribute to each p^* bin at most momenta. At low p^*/m_{had}, this increases to as many as 9 bins for 0.3 GeV/c protons in $\theta6$.

The matrix $\mathbf{W}$ is sensitive to the shape of the true p^* distribution, and the transformation is incorrect if that is not modeled well. The effect is small (zero) if the distribution varies smoothly (linearly) over the relevant p^* range, but can be large near a peak or inflection point and at high p^* where distributions fall exponentially. We use an iterative procedure in which we reweight the simulation to match the measured distribution, redo the transformation, and repeat until the changes are sufficiently small. This procedure is reliable if the initial differences are not too large. In each case we find a measured p^* distribution with statistically significant differences in shape from the simulation, but the first iteration produces changes smaller than the statistical uncertainties, and changes from the second iteration are negligible. We assign no systematic uncertainty from this source.

$\mathbf{W}$ is insensitive to the true $\cos\theta^*$ distribution, whereas the F_j are quite sensitive to $\cos\theta^*$ but almost insensitive to the true p^* distribution. The $\cos\theta^*$ distribution must therefore be modeled sufficiently well. It has the approximate form $D(\cos\theta^*) \propto 1 + a(p^*)\cos^2\theta^*$ with $0 < a(p^*) < 1$, where $a(p^*)$ is small for low p^* but approaches 1 for high p^*. We compare the cross sections σ_i measured in the six $\cos\theta_{lab}$ regions, which are shown for the on-resonance data in Fig. 8 divided by their weighted average value (see below) in each p^* bin. The uncertainties are statistical only, and are correlated with their 2–3 nearest neighbors as a result of the transformation to the CM frame. The solid (dashed) lines indicate (twice) the root-mean-square (RMS) variation expected from the
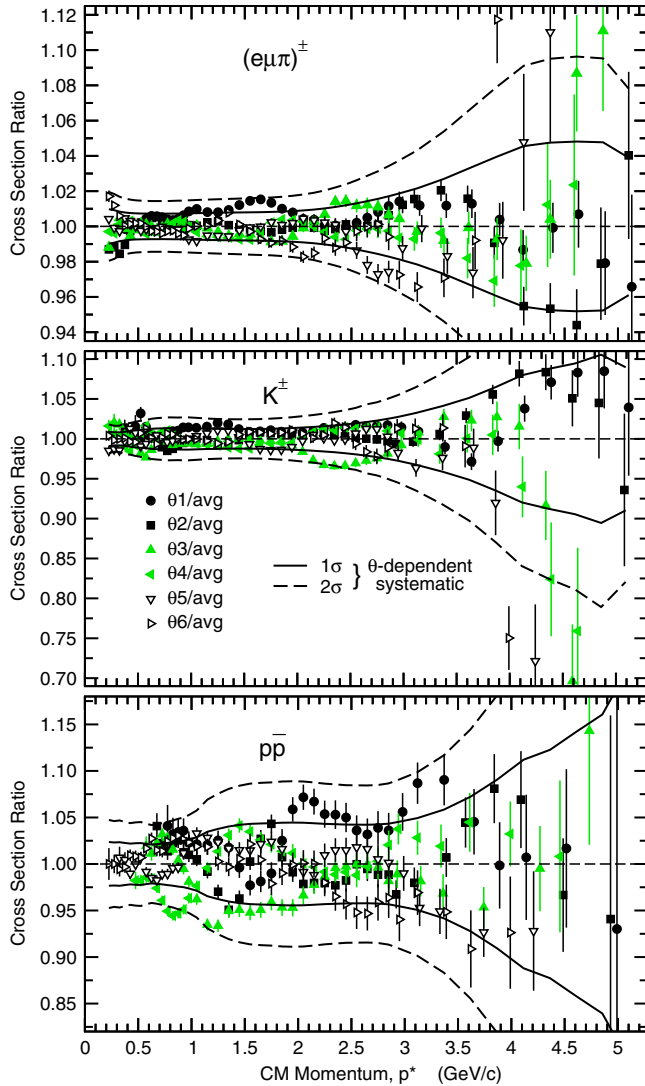
FIG. 8 (color online). Ratios of fully corrected cross sections from each $\cos\theta_{\mathrm{lab}}$ region to their average value. The error bars are statistical only, and some bins have been combined for clarity. The solid and dashed lines indicate the variations expected at one and two standard deviations, respectively.

systematic uncertainties discussed so far. The largest contribution to this is from the particle identification efficiencies, which are evaluated independently in each $\cos\theta_{\mathrm{lab}}$ region, but are correlated over ranges of several p^* bins. Below 0.5 GeV/c, uncertainties of the tracking efficiency are also important; these are similar among $\cos\theta_{\mathrm{lab}}$ regions for a given p_{lab} value, but vary at a given p^*, and are correlated within each $\cos\theta_{\mathrm{lab}}$ region.

Overall, the data are consistent within the expected variation, and the off-resonance data show a similar set of variations. An incorrectly simulated $a(p^*)$ would be visible here as a specific pattern of differences between the σ_i at that p^*, roughly parabolic in i with $\sigma_1 > \sigma_2 \approx \sigma_6 > \sigma_3 \approx \sigma_5 > \sigma_4$ (or the reverse). The amplitude of this

pattern would be expected to vary slowly with p^* over several bins, or perhaps across the full range. No such pattern is visible in Fig. 8, and we set limits on any mismodeling by fitting the expected pattern to the σ_i in each p^* bin. For each particle we find the largest amplitude averaged over three neighboring p^* bins. They correspond to 0.5%, 1% and 2% shifts in σ_1, or 1%, 2% and 4% spreads between the $\theta 1$ and $\theta 4$ points in Fig. 8, for pions, kaons and protons, respectively. We take these limiting shifts in σ_1 as conservative systematic uncertainties in each region and at all p^*. The corresponding shifts in the other σ_i are smaller, and those in σ_3, σ_4 and σ_5 are of opposite sign; we take this correlation into account in the average, leading to a partial cancellation.

This comparison also limits several other systematic effects. For example, it is sensitive to an incorrect boost value, which would give $\sigma_1 > \sigma_2 > \sigma_3 > \sigma_4 > \sigma_5 > \sigma_6$ with the differences increasing linearly with p^*; the data limit any such effect to a negligible level. A poor simulation of material interactions or soft-track efficiencies would appear as a spread in the σ_i, with a particular ordering, as p^* approaches its lowest value. We observe up to 6% spreads without the corrections described in Sec. V C, but no significant spread is visible in Fig. 8. In the $K^\pm$ plot, the highest-p^* points for $\theta 3$–$\theta 6$ are low. This may be due to a systematic effect in the kaon identification efficiencies, but the uncertainties for these points are large and they contribute little to the average. We check for the characteristic ordering and p^* dependence expected from residual mismodeling of the p^* distribution, and we observe no significant effects.

In each p^* bin, we average the values from the $\cos\theta_{\mathrm{lab}}$ regions weighted by their total uncertainties. Due to the low identification efficiencies at high p_{lab}, some measurements have very large uncertainties, and we do not use the data above p^* values of 5.00, 4.75, 4.50, and 4.25 GeV/c in $\theta 3$, $\theta 4$, $\theta 5$, and $\theta 6$, respectively. The uncertainties are relatively large just below these cutoff points, so that the high-p^* measurements are dominated by the backward regions where the momenta are boosted downward and identification efficiencies are high. Low-p^* protons are boosted very far forward, and only $\theta 6$ contributes below 0.30 GeV/c, with $\theta 5$, $\theta 4$, $\theta 3$, $\theta 2$, and $\theta 1$ starting at 0.30, 0.45, 0.60, 0.70, and 0.75 GeV/c. Three (five) regions contribute to the lowest-p^* kaon (pion) point, with the others coming in at 0.25, 0.35, and 0.45 GeV/c (0.30 GeV/c). All six regions contribute over most of the p^* range.

The particle-identification uncertainties in different $\cos\theta_{\mathrm{lab}}$ regions are independent of each other, since they are derived from distinct control samples. These and the statistical uncertainties are therefore reduced according to the number of regions contributing to the average in each p^* bin. The uncertainties due to the $\cos\theta^*$ distributions are common to all $\cos\theta^*$ regions, but are anticorrelated

between the central and forward/backward regions, so they are also reduced accordingly. We take all other uncertainties to be completely correlated between the regions and average them, but the weighting takes advantage of the variations with p_{lab} and/or $\cos\theta_{lab}$.

E. Cross sections for prompt and conventional hadrons

The leptons in the $(e\mu\pi)^{\pm}$ cross section are from the decays of hadrons produced in the fragmentation process, such as Dalitz decays of π^0 and semileptonic decays of D hadrons. This cross section is included in the Supplemental Material [38]; we now subtract the leptons to obtain the $\pi^{\pm}$ cross section. We show our simulated $e^{\pm}$, $\mu^{\pm}$, and total lepton contributions as fractions of the $(e\mu\pi)^{\pm}$ cross section in Fig. 9. Charmed hadron decays produce most of the leptons, with a maximum contribution of 4% near 1.5 GeV/c, and π^0 decays produce most of the $e^{\pm}$ at low p^*.

The π^0 cross section has been measured in $e^+e^- \rightarrow q\bar{q}$ events at higher energies [29], and the simulation reproduces these results to within 10%. Charmed hadron spectra in $e^+e^- \rightarrow q\bar{q}$ events have been measured well at our E_{CM} [39–41]. Our simulated spectra are slightly too soft, which has a small effect on the peak positions in the lepton spectra. Of greater concern is the variation in peak position among different charmed hadrons, whose relative production rates are uncertain at the few percent level [29]. We subtract the simulated fractional lepton contributions and assign a set of systematic uncertainties sufficient to cover all these effects. We vary the normalization of the π^0 contribution by $\pm10\%$, and consider an independent shape variation by reweighting the π^0 distribution linearly in p^* so as to change the contribution by $\pm50\%$ at 0.5 GeV/c. We assign a 10% normalization uncertainty to the charm decay contribution, and also consider a shift in the peak position of ±0.2 GeV/c.

The resulting differential cross sections for prompt particles are shown in Fig. 10. The statistical uncertainties are

FIG. 10. Differential production cross sections for prompt (filled symbols) and conventional (open symbols) $\pi^{\pm}$ (circles), $K^{\pm}$ (squares) and $p/\bar{p}$ (diamonds) per $e^+e^- \rightarrow q\bar{q}$ event as functions of p^*. The insets show the high momentum regions with expanded vertical scales. The prompt and conventional $K^{\pm}$ cross sections are indistinguishable.

smaller than the symbol size, and systematic uncertainties are discussed in the next subsection. Our measurement covers the bulk of the kaon and proton spectra, as well as the peak and high side of the pion spectrum.

We calculate cross sections for the conventional set of decay chains by including the simulated contributions from K_S^0 and strange baryon decays, reweighted and with uncertainties as described in Sec. V B. These conventional cross sections are also shown in Fig. 10. The prompt and conventional $K^{\pm}$ cross sections are indistinguishable, since the dominant difference is from decays of Ω^- baryons, which are produced at a very low rate. The other cross sections converge at high p^* where decays cannot contribute. The conventional $\pi^{\pm}$ cross section is a few percent higher overall than the prompt cross section due to K_S^0 decays, and as much as 13% higher at the lowest p^* due to strange baryon decays. The conventional $p/\bar{p}$ cross section is 50% higher over much of the range, due to strange baryon decays.

F. Summary of systematic uncertainties

Most of the systematic uncertainties and checks are described above. We also consider possible mismodeling of the absolute event selection efficiency by varying the
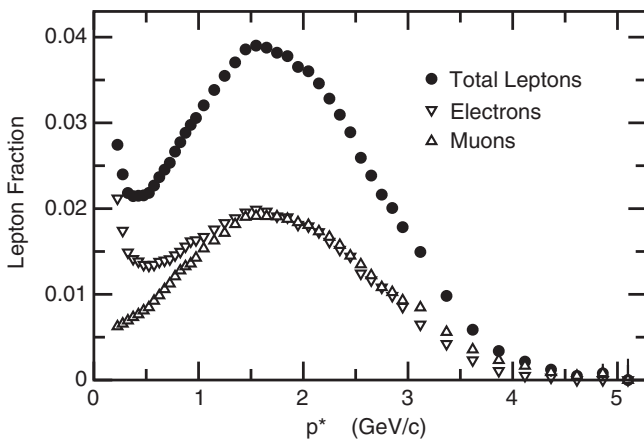

FIG. 9. Simulated electron (down triangles), muon (up triangles) and total lepton (circles) cross sections divided by the $(e\mu\pi)$ cross section in $e^+e^- \rightarrow q\bar{q}$ events as functions of p^*.
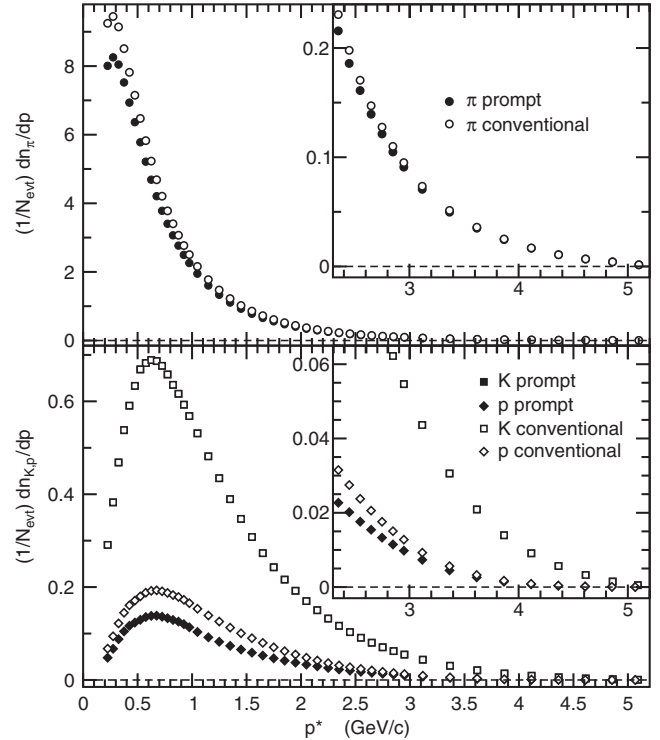
selection criteria described in Sec. III and using alternative event generators. We find negligible changes in the shapes of the cross sections, but some of the variations give changes in the overall normalization of 0.3%–0.5%. We assign an overall uncertainty of 0.5%, corresponding to the largest variation seen. We also propagate statistical uncertainties on simulated quantities as a category of systematic uncertainty.

We summarize the relative uncertainties on our cross sections in Fig. 11. A few become large at high p^*, where the cross sections become low, and we do not show those that are off the vertical scale. The statistical uncertainties are much smaller than the systematic uncertainties except at the highest p^* values, and on the lowest-p^* $p/\bar{p}$ points. The samples with full detector simulation are similar in size to the data samples, and the corresponding uncertainties (not shown) are the largest systematic uncertainties at the highest p^* values. The total uncertainties are as small as 1.2%, 1.4%, and 3.2% (1.3%, 1.4%, and 3.6%) for prompt (conventional) $\pi^\pm$, $K^\pm$ and $p/\bar{p}$, respectively, in the 0.6–0.8 GeV/c range. They increase at lower p^* due mostly to tracking efficiency, and at higher p^* due to particle identification and backgrounds. The latter are

dominated by τ-pairs for $\pi^\pm$ and $K^\pm$, and by strange decays for $p/\bar{p}$.

All of the systematic uncertainties have strong point-to-point correlations. There is an overall normalization uncertainty of 0.98% from the event selection and part of the track-finding efficiency, which does not affect the shape of any cross section. The uncertainties due to most backgrounds, strange particle decays, $\cos \theta^*$ distributions, and leptons are correlated over wide ranges, and can have broad effects on the shape. Those due to particle identification are correlated strongly over short ranges, typically ± 1–2 neighboring bins, and more weakly over ± 2–4 additional bins, and the simulation has been smoothed so that its statistical uncertainty is correlated over 4–6 bins. These can lead to apparent structures in the cross sections over ranges of several bins. The remaining uncertainties on the tracking efficiencies and those due to interactions in the detector material (radiative Bhabha background) are fully correlated over the entire p^* range, but are non-negligible only in the 6–10 lowest (highest) p^* bins. Overall, the correlation coefficients for neighboring bins are 92%–99% near the centers of the measured ranges and 72%–96% (15%–73%) toward the low-p^* (high-p^*) end. They are over 50% for bin separations of 12 or fewer. The full correlation matrices are given in the Supplemental Material [38].

VI. RESULTS AND INTERPRETATION

Our results for prompt and conventional hadrons are listed in Tables I and II. Several other tables, including breakdowns of the uncertainties and their correlations, are available in the Supplemental Material [38]. In this section, we compare the cross section results with previous measurements, models of hadronization, and predictions of QCD. We also calculate average event multiplicities, ratios of differential production cross sections, and charged hadron fractions.

A. Cross sections in $e^+ e^- \rightarrow q\bar{q}$ events

We compare our results with previous measurements from the ARGUS experiment [11] of differential $\pi^\pm$, $K^\pm$ and $p/\bar{p}$ production cross sections in $e^+ e^- \rightarrow q\bar{q}$ events at the slightly lower $E_{CM} = 9.98$ GeV. Figure 12 shows their tabulated results for prompt particles, along with ours, in terms of the scaled momentum $x_p = 2p^*/E_{CM}$, over the range of their measurements. Total uncertainties are shown for both data sets. Although our results are far more precise statistically, the systematic uncertainties are comparable and are correlated over significant x_p ranges in both cases. The ARGUS $\pi^\pm$ and $K^\pm$ data extend to lower x_p values, whereas ours extend up to $x_p = 1$, so that most of the relevant range is covered between the two experiments.

For $x_p > 0.1$, the two data sets are consistent. As x_p decreases, the ARGUS data fall systematically below ours,
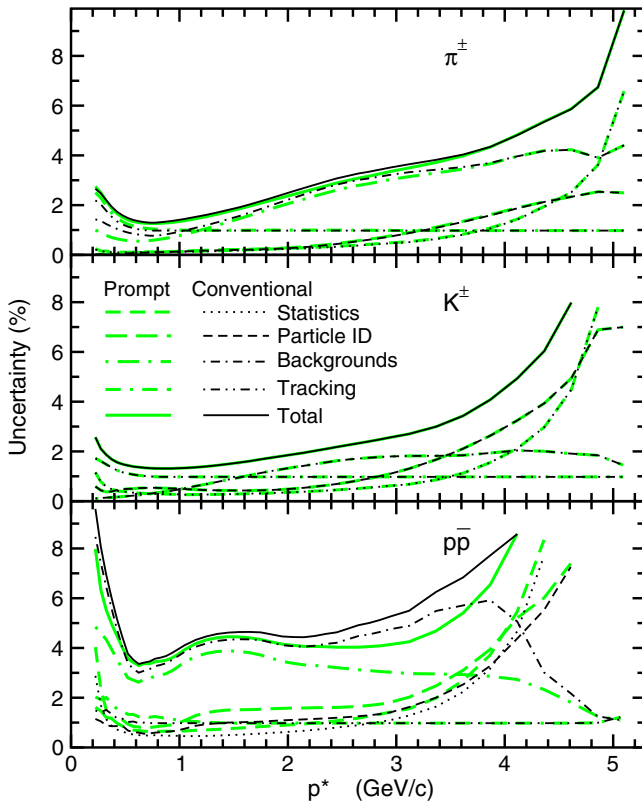

FIG. 11 (color online). Relative uncertainties in percent on the differential production cross sections for prompt (gray/green) and conventional (black) $\pi^\pm$ (top), $K^\pm$ (middle) and $p/\bar{p}$ (bottom) as functions of p^*. The totals are shown along with several important components. Some uncertainties become large at high p^*, and are not shown.

TABLE I.   Differential cross sections for prompt $\pi^\pm$, $K^\pm$ and $p/\bar{p}$ in $e^+e^- \to q\bar{q}$ events, along with their totals over the measured range. The first uncertainties are statistical (stat.) and the second systematic (syst.). The 0.98% normalization uncertainty is not included, except on the totals.

Momentum range (GeV/c)	$(1/N_{\text{evt}})dn_\pi/dp$ Value	Stat.	Syst.	$(1/N_{\text{evt}})dn_K/dp$ Value	Stat.	Syst.	$(1/N_{\text{evt}})dn_p/dp$ Value	Stat.	Syst.
0.20–0.25	8.01	±0.02	±0.22	0.291	±0.003	±0.007	0.0479	±0.0019	±0.0033
0.25–0.30	8.25	±0.01	±0.21	0.382	±0.003	±0.007	0.0672	±0.0016	±0.0040
0.30–0.35	8.04	±0.01	±0.17	0.468	±0.003	±0.008	0.0879	±0.0013	±0.0047
0.35–0.40	7.52	±0.01	±0.14	0.538	±0.003	±0.009	0.1046	±0.0012	±0.0050
0.40–0.45	6.93	±0.01	±0.11	0.591	±0.002	±0.009	0.1167	±0.0011	±0.0051
0.45–0.50	6.36	±0.01	±0.10	0.633	±0.002	±0.009	0.1237	±0.0011	±0.0048
0.50–0.55	5.78	±0.01	±0.08	0.669	±0.002	±0.009	0.1296	±0.0010	±0.0045
0.55–0.60	5.21	±0.01	±0.07	0.682	±0.002	±0.009	0.1356	±0.0009	±0.0045
0.60–0.65	4.69	±0.01	±0.06	0.689	±0.002	±0.009	0.1380	±0.0009	±0.0044
0.65–0.70	4.21	±0.01	±0.05	0.687	±0.002	±0.009	0.1384	±0.0009	±0.0046
0.70–0.75	3.781	±0.005	±0.048	0.676	±0.002	±0.009	0.1363	±0.0009	±0.0045
0.75–0.80	3.402	±0.004	±0.043	0.658	±0.002	±0.008	0.1331	±0.0009	±0.0045
0.80–0.85	3.065	±0.004	±0.039	0.636	±0.002	±0.008	0.1292	±0.0008	±0.0044
0.85–0.90	2.765	±0.004	±0.035	0.616	±0.002	±0.008	0.1256	±0.0008	±0.0043
0.90–0.95	2.495	±0.003	±0.032	0.593	±0.002	±0.008	0.1200	±0.0008	±0.0042
0.95–1.00	2.258	±0.003	±0.030	0.568	±0.002	±0.007	0.1135	±0.0008	±0.0041
1.00–1.10	1.948	±0.002	±0.027	0.531	±0.001	±0.007	0.1033	±0.0007	±0.0040
1.10–1.20	1.603	±0.002	±0.023	0.482	±0.001	±0.006	0.0919	±0.0006	±0.0038
1.20–1.30	1.332	±0.002	±0.020	0.435	±0.001	±0.006	0.0823	±0.0006	±0.0035
1.30–1.40	1.106	±0.002	±0.018	0.389	±0.001	±0.006	0.0734	±0.0005	±0.0032
1.40–1.50	0.926	±0.002	±0.016	0.347	±0.001	±0.005	0.0655	±0.0005	±0.0029
1.50–1.60	0.780	±0.002	±0.014	0.3080	±0.0009	±0.0047	0.0588	±0.0005	±0.0026
1.60–1.70	0.659	±0.001	±0.013	0.2731	±0.0008	±0.0043	0.0526	±0.0004	±0.0023
1.70–1.80	0.559	±0.001	±0.012	0.2427	±0.0008	±0.0040	0.0466	±0.0004	±0.0020
1.80–1.90	0.475	±0.001	±0.010	0.2161	±0.0007	±0.0037	0.0416	±0.0004	±0.0017
1.90–2.00	0.404	±0.001	±0.009	0.1921	±0.0007	±0.0034	0.0374	±0.0003	±0.0015
2.00–2.10	0.343	±0.001	±0.008	0.1698	±0.0006	±0.0031	0.0331	±0.0003	±0.0013
2.10–2.20	0.294	±0.001	±0.007	0.1503	±0.0006	±0.0029	0.0293	±0.0003	±0.0012
2.20–2.30	0.251	±0.001	±0.007	0.1323	±0.0005	±0.0026	0.0259	±0.0003	±0.0010
2.30–2.40	0.216	±0.001	±0.006	0.1167	±0.0005	±0.0024	0.0227	±0.0002	±0.0009
2.40–2.50	0.186	±0.001	±0.005	0.1031	±0.0005	±0.0022	0.0201	±0.0002	±0.0008
2.50–2.60	0.1610	±0.0006	±0.0048	0.0909	±0.0004	±0.0020	0.0176	±0.0002	±0.0007
2.60–2.70	0.1394	±0.0005	±0.0043	0.0802	±0.0004	±0.0018	0.0154	±0.0002	±0.0006
2.70–2.80	0.1213	±0.0005	±0.0038	0.0704	±0.0004	±0.0016	0.0133	±0.0002	±0.0005
2.80–2.90	0.1048	±0.0005	±0.0034	0.0622	±0.0004	±0.0015	0.01146	±0.00015	±0.00044
2.90–3.00	0.0910	±0.0004	±0.0030	0.0546	±0.0003	±0.0014	0.00979	±0.00014	±0.00038
3.00–3.25	0.0706	±0.0004	±0.0024	0.0436	±0.0003	±0.0011	0.00733	±0.00011	±0.00029
3.25–3.50	0.0497	±0.0003	±0.0018	0.0306	±0.0003	±0.0009	0.00448	±0.00009	±0.00019
3.50–3.75	0.0350	±0.0003	±0.0014	0.0209	±0.0002	±0.0007	0.00260	±0.00007	±0.00012
3.75–4.00	0.0246	±0.0003	±0.0010	0.0139	±0.0002	±0.0005	0.00143	±0.00005	±0.00008
4.00–4.25	0.0167	±0.0002	±0.0008	0.00910	±0.00019	±0.00041	0.00073	±0.00004	±0.00005
4.25–4.50	0.0107	±0.0002	±0.0005	0.00568	±0.00017	±0.00030	0.00036	±0.00003	±0.00003
4.50–4.75	0.00681	±0.00017	±0.00036	0.00324	±0.00015	±0.00021	0.00017	±0.00002	±0.00002
4.75–5.00	0.00418	±0.00015	±0.00024	0.00149	±0.00012	±0.00015	0.00007	±0.00002	±0.00001
5.00–5.27	0.00153	±0.00010	±0.00011	0.00050	±0.00007	±0.00007	0.00001	±0.00001	±0.00001
0.20–5.27	5.364	±0.002	±0.080	0.946	±0.001	±0.012	0.1819	±0.0003	±0.0058

TABLE II.   Differential cross sections for conventional $\pi^{\pm}$, $K^{\pm}$ and $p/\bar{p}$ in $e^+e^- \to q\bar{q}$ events, along with their totals over the measured range. The first uncertainties are statistical (stat.) and the second systematic (syst.). The 0.98% normalization uncertainty is not included, except on the totals.

| Momentum range (GeV/c)	$(1/N_{\mathrm{evt}})dn_{\pi}/dp$			$(1/N_{\mathrm{evt}})dn_{K}/dp$			$(1/N_{\mathrm{evt}})dn_{p}/dp$		
	Value	Stat.	Syst.	Value	Stat.	Syst.	Value	Stat.	Syst.
0.20–0.25	9.25	±0.02	±0.24	0.291	±0.003	±0.007	0.068	±0.002	±0.006
0.25–0.30	9.45	±0.01	±0.23	0.383	±0.003	±0.007	0.094	±0.002	±0.007
0.30–0.35	9.14	±0.01	±0.20	0.468	±0.003	±0.008	0.122	±0.001	±0.008
0.35–0.40	8.51	±0.01	±0.16	0.538	±0.003	±0.009	0.145	±0.001	±0.009
0.40–0.45	7.82	±0.01	±0.14	0.591	±0.002	±0.009	0.161	±0.001	±0.008
0.45–0.50	7.15	±0.01	±0.11	0.633	±0.002	±0.009	0.171	±0.001	±0.007
0.50–0.55	6.47	±0.01	±0.10	0.669	±0.002	±0.009	0.180	±0.001	±0.007
0.55–0.60	5.83	±0.01	±0.08	0.683	±0.002	±0.009	0.188	±0.001	±0.007
0.60–0.65	5.23	±0.01	±0.07	0.689	±0.002	±0.009	0.192	±0.001	±0.006
0.65–0.70	4.69	±0.01	±0.06	0.687	±0.002	±0.009	0.193	±0.001	±0.007
0.70–0.75	4.21	±0.01	±0.05	0.677	±0.002	±0.009	0.191	±0.001	±0.007
0.75–0.80	3.778	±0.004	±0.049	0.658	±0.002	±0.008	0.187	±0.001	±0.007
0.80–0.85	3.401	±0.004	±0.044	0.636	±0.002	±0.008	0.183	±0.001	±0.007
0.85–0.90	3.067	±0.004	±0.041	0.616	±0.002	±0.008	0.179	±0.001	±0.007
0.90–0.95	2.768	±0.003	±0.038	0.593	±0.002	±0.008	0.173	±0.001	±0.006
0.95–1.00	2.504	±0.003	±0.035	0.568	±0.002	±0.007	0.165	±0.001	±0.006
1.00–1.10	2.159	±0.003	±0.031	0.531	±0.001	±0.007	0.153	±0.001	±0.006
1.10–1.20	1.775	±0.002	±0.027	0.482	±0.001	±0.006	0.139	±0.001	±0.006
1.20–1.30	1.472	±0.002	±0.024	0.435	±0.001	±0.006	0.126	±0.001	±0.006
1.30–1.40	1.221	±0.002	±0.021	0.389	±0.001	±0.006	0.113	±0.001	±0.005
1.40–1.50	1.020	±0.002	±0.018	0.347	±0.001	±0.005	0.1006	±0.0005	±0.0046
1.50–1.60	0.857	±0.002	±0.016	0.3080	±0.0009	±0.0047	0.0900	±0.0005	±0.0042
1.60–1.70	0.723	±0.001	±0.015	0.2731	±0.0008	±0.0043	0.0799	±0.0004	±0.0037
1.70–1.80	0.611	±0.001	±0.013	0.2427	±0.0008	±0.0040	0.0704	±0.0004	±0.0032
1.80–1.90	0.518	±0.001	±0.012	0.2161	±0.0007	±0.0037	0.0620	±0.0004	±0.0028
1.90–2.00	0.439	±0.001	±0.011	0.1921	±0.0007	±0.0034	0.0548	±0.0003	±0.0024
2.00–2.10	0.372	±0.001	±0.009	0.1698	±0.0006	±0.0031	0.0480	±0.0003	±0.0021
2.10–2.20	0.317	±0.001	±0.008	0.1503	±0.0006	±0.0029	0.0419	±0.0003	±0.0018
2.20–2.30	0.270	±0.001	±0.008	0.1323	±0.0005	±0.0026	0.0364	±0.0003	±0.0016
2.30–2.40	0.231	±0.001	±0.007	0.1167	±0.0005	±0.0024	0.0315	±0.0002	±0.0014
2.40–2.50	0.198	±0.001	±0.006	0.1031	±0.0005	±0.0022	0.0275	±0.0002	±0.0012
2.50–2.60	0.170	±0.001	±0.005	0.0909	±0.0004	±0.0020	0.0237	±0.0002	±0.0011
2.60–2.70	0.1471	±0.0006	±0.0048	0.0802	±0.0004	±0.0018	0.0206	±0.0002	±0.0010
2.70–2.80	0.1276	±0.0005	±0.0042	0.0704	±0.0004	±0.0016	0.0176	±0.0002	±0.0009
2.80–2.90	0.1099	±0.0005	±0.0037	0.0622	±0.0004	±0.0015	0.0150	±0.0002	±0.0008
2.90–3.00	0.0950	±0.0004	±0.0033	0.0546	±0.0003	±0.0014	0.0128	±0.0001	±0.0007
3.00–3.25	0.0734	±0.0004	±0.0026	0.0436	±0.0003	±0.0011	0.00926	±0.00012	±0.00049
3.25–3.50	0.0513	±0.0003	±0.0019	0.0306	±0.0003	±0.0009	0.00564	±0.00009	±0.00034
3.50–3.75	0.0359	±0.0003	±0.0014	0.0209	±0.0002	±0.0007	0.00324	±0.00007	±0.00021
3.75–4.00	0.0251	±0.0003	±0.0011	0.0139	±0.0002	±0.0005	0.00173	±0.00005	±0.00012
4.00–4.25	0.0169	±0.0002	±0.0008	0.00910	±0.00019	±0.00041	0.00087	±0.00004	±0.00006
4.25–4.50	0.0108	±0.0002	±0.0005	0.00568	±0.00017	±0.00030	0.00040	±0.00003	±0.00003
4.50–4.75	0.00682	±0.00017	±0.00036	0.00324	±0.00015	±0.00021	0.00017	±0.00002	±0.00002
4.75–5.00	0.00418	±0.00015	±0.00024	0.00149	±0.00012	±0.00015	0.00007	±0.00002	±0.00001
5.00–5.27	0.00153	±0.00010	±0.00011	0.00050	±0.00007	±0.00007	0.00001	±0.00001	±0.00001
0.20–5.27	6.002	±0.002	±0.092	0.946	±0.001	±0.012	0.2612	±0.0003	±0.0095
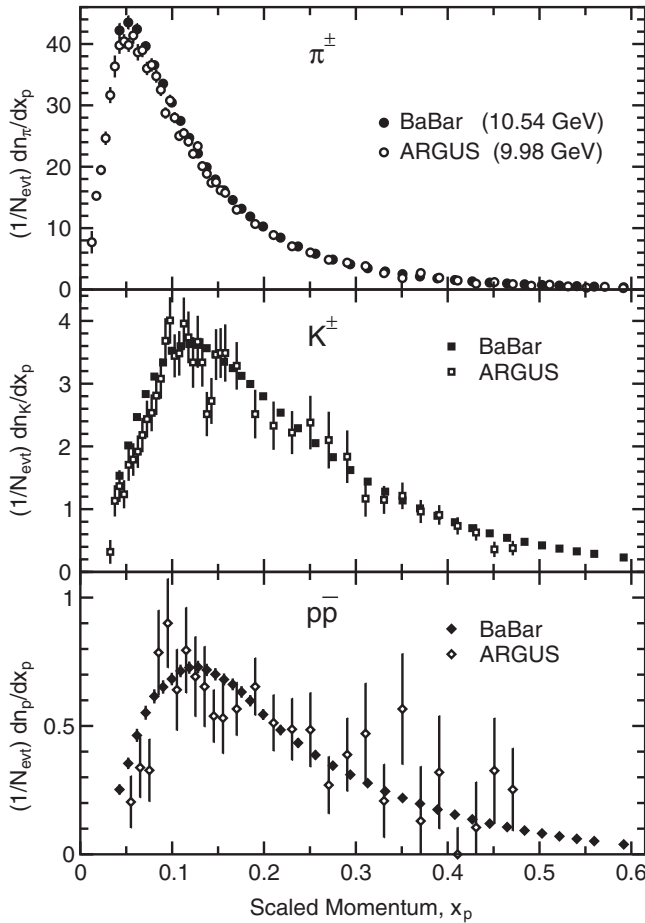
FIG. 12. Comparison of our differential cross sections for prompt $\pi^\pm$ (top), $K^\pm$ (middle) and $p/\bar{p}$ (bottom) with previous results from ARGUS at $\sqrt{s} = 9.98$ GeV. The error bars represent combined statistical and systematic uncertainties.

as might be expected from a mass-driven scaling violation. The differences are consistent with those expected by the hadronization models described in Sec. VI B. However, when the correlations between the systematic uncertainties are taken into account, the significance of these differences is only a few standard deviations for $\pi^\pm$ and $K^\pm$, and below 2σ for $p/\bar{p}$. ARGUS also presents results including K_S^0 and Λ decay products. A comparison with our conventional results yields the same conclusions.

B. Comparison with hadronization models

In Fig. 13, we compare our cross sections for prompt particles with the predictions of the three hadronization models discussed in Sec. I. These models represent the three different mechanisms for hadronization currently available. In each case we use the default parameter values, which have been chosen based on previous data, mostly at higher energies but including the ARGUS data. All three models describe the bulk of the spectra qualitatively, but no model describes any spectrum in detail. The peak positions
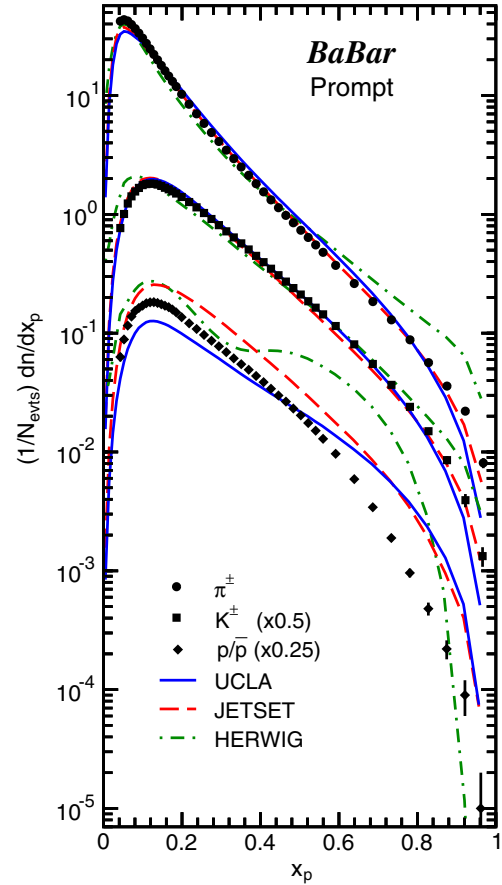
FIG. 13 (color online). Comparison of the prompt $\pi^\pm$ (circles), $K^\pm$ (squares) and $p/\bar{p}$ (diamonds) cross sections in $e^+e^- \to q\bar{q}$ events with the predictions of the UCLA (solid line), JETSET (dashed) and HERWIG (dotted) hadronization models.

are consistent with the data, except for the HERWIG $K^\pm$, which is too low. The peak amplitudes are low by 9%–20% for $\pi^\pm$, high by 8%–11% for $K^\pm$, and either 30% low or 30%–50% high for $p/\bar{p}$.

The HERWIG peaks are too narrow, and the high-x_p tails are much too long; in particular, the $p/\bar{p}$ spectrum shows a pronounced structure at high x_p, and also drops to zero in the highest-x_p bin. In contrast, the JETSET and UCLA $\pi^\pm$ and $K^\pm$ peaks are slightly too broad, and the tails too short, although both models describe the shape well in the 0.2–0.7 range. UCLA also reproduces the amplitude of the $K^\pm$ spectrum in this range. JETSET's $p/\bar{p}$ spectrum has the correct shape for $x_p < 0.5$, but then drops too slowly. UCLA's $p/\bar{p}$ spectrum is distorted relative to the data in a manner similar to HERWIG's $\pi^\pm$ and $K^\pm$ spectra. A comparison of the conventional cross sections (not shown) gives similar results.

Similar discrepancies with these models have been reported at higher energies [12–18], although earlier versions of the models were often used and some parameter values differed. Most differences from the data were of the same sign and similar in size to those we observe,

suggesting that the scaling with E_{CM} might be well simulated. In some cases, simple changes to parameters in JETSET produced improvements in the agreement with data, and some experiments implemented global tuning. We do not attempt to tune any of the models, but we test some simple modifications of JETSET parameters: changing the probability of producing a diquark-antidiquark rather than a $q\bar{q}$ pair at each string break modifies the amplitude of the simulated proton spectrum, but does not change the shape; similarly, the probability to produce an $s\bar{s}$ rather than $u\bar{u}$ or $d\bar{d}$ pair controls the amplitude, but not the shape, of the kaon spectrum.

We test the scaling properties of the models by generating samples with each at various energies, comparing them with available data, and looking for changes in the type or magnitude of any differences. In the top plot in Fig. 14 we show our conventional $\pi^{\pm}$ cross section along with those from the TASSO and SLD experiments. At high x_p, these two experiments provide the most precise data and/or widest coverage for E_{CM} near 30 GeV and the Z^0 peak. Data from other experiments are consistent and yield the same conclusions, but are omitted for clarity. Strong scaling violations are evident, both at low x_p due to the pion mass and at high x_p as expected from the running of the strong coupling strength α_s. Also shown are the predictions of the JETSET model at these three energies, using default parameter values. JETSET provides a good description of all three data sets for $x_p > 0.2$, and hence describes the high-x_p scaling violation well. The other two models also reproduce this E_{CM} dependence, though they do not describe the spectrum well at any energy.

The middle plot in Fig. 14 shows a similar test for the $K^{\pm}$ cross section. Here we show the UCLA model predictions, as they describe our results best at high x_p. The different flavor composition of the three samples is important for $K^{\pm}$ and modifies the expected scaling violation. Kaons from $b\bar{b}$ events, which are absent from our data, contribute strongly to the TASSO cross section in the 0.1–0.3 region, but little at higher x_p. Since the cross sections are normalized per event, the expected scaling violation is reduced relative to that in the $\pi^{\pm}$ cross sections in the 0.1–0.3 range, and increased at higher x_p. At the Z^0 energy, the relative production of up- and down-type quarks is quite different, and the combination of more $K^{\pm}$ from $b\bar{b}$ and $s\bar{s}$ events and fewer from $c\bar{c}$ events pushes the simulated high-x_p cross section up to nearly the same level as for the TASSO energy.

The flavor dependence has been shown [15,18] to be accurately modeled at the Z^0 energy to the level of about 10%. The UCLA model describes the shape of the SLD cross section at high x_p well, but is too low by about 15%. The other models also predict about 15% more scaling violation than is observed. However, it is difficult to draw any conclusion in light of the flavor dependence.
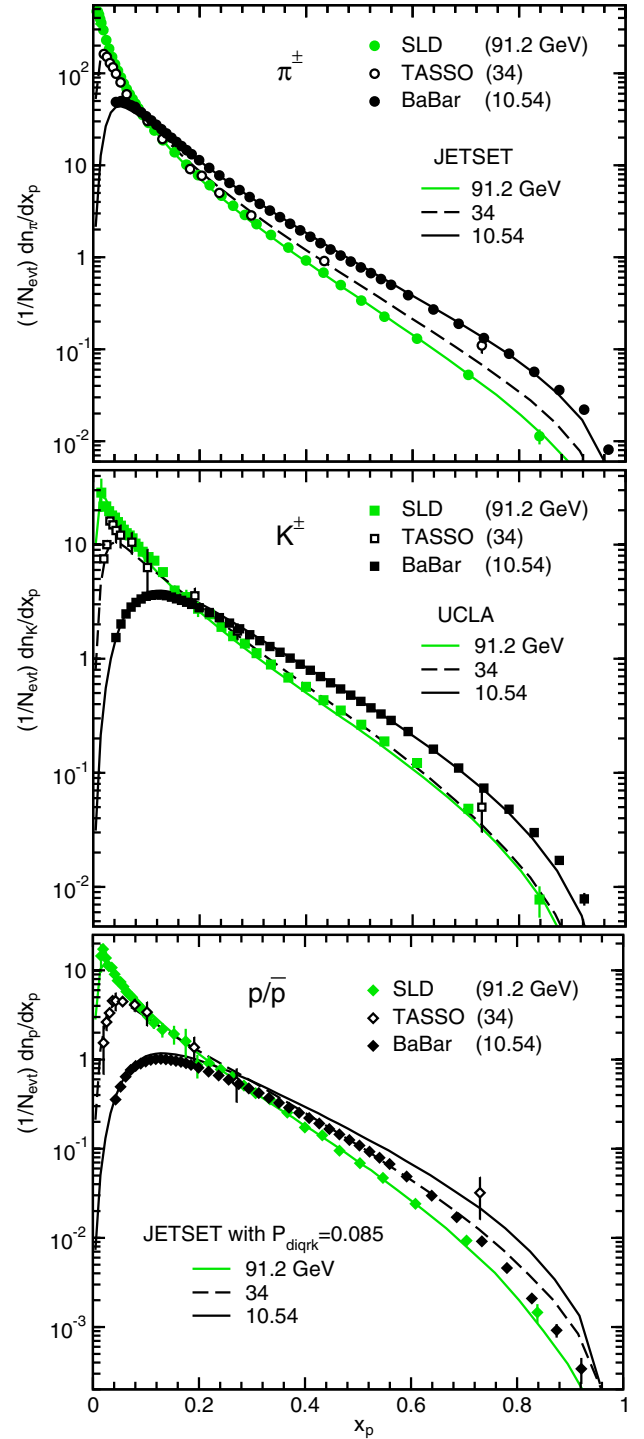

FIG. 14 (color online).   Conventional $\pi^{\pm}$ (top), $K^{\pm}$ (middle) and $p/\bar{p}$ (bottom) cross sections measured at three different CM energies, compared with the predictions of the simulations described in the text.

For protons, shown in the bottom plot in Fig. 14, we compare with the JETSET model in which we have changed one parameter value, the diquark production probability P_{diqrk}, from 0.1 to 0.085. This provides a good description of the SLD and TASSO data at all x_p, although the latter

are sparse at high x_p. The simulated high-x_p scaling violation between 10.54 and 34 GeV is similar to that for $\pi^\pm$, but that between 34 and 91 GeV is slightly larger since fast protons are expected to be produced predominantly in $u\bar{u}$ and $d\bar{d}$ events. The prediction for 10.54 GeV is consistent with the *BABAR* data for x_p below 0.07, but then rises well above the data, exceeding it by as much as a factor of 3 at $x_p = 0.8$. We see similar behavior for JETSET with default parameter values, HERWIG, and UCLA. Thus none of these models predicts the correct scaling properties for protons, even though they describe the properties of pions well.

C. Tests of MLLA QCD

We test the predictions of QCD in the modified leading logarithm approximation (MLLA) [3], combined with the ansatz of local parton-hadron duality (LPHD) [3], using our cross sections in the variable $\xi = -\ln(x_p)$. Figure 15 shows the ξ distributions for prompt particles; the conventional distributions are similar in shape. The error bars are statistical. Because of their strong correlations, the systematic uncertainties are shown as bands. The normalization uncertainty is not included, as it does not affect the shapes.

This representation emphasizes the low-p^* (large ξ) region and most of each spectrum is visible on a linear vertical scale. The spectra exhibit slow rises from zero at $\xi = 0$ (the beam momentum) and the "humpbacked plateau" predicted by MLLA + LPHD. The MLLA + LPHD hypothesis also predicts that Gaussian functions should describe these spectra over ranges of ± 0.5–1 units about the peak position ξ^*, and that slightly distorted Gaussian functions should fit the data over substantially wider ranges. Furthermore, ξ^* should decrease exponentially with increasing hadron mass at a given E_{CM}, and increase logarithmically with E_{CM} for a given hadron type.

Following convention, we first estimate ξ^* by fitting Gaussian functions over a set of ξ ranges each about one unit wide and centered within one bin of the peak. Given our binning, we consider nine such ranges for $\pi^\pm$, and four for $K^\pm$ and $p/\bar{p}$. We average the mean values and statistical and systematic uncertainties of the set of fits, and include the RMS deviation among the means as an additional systematic uncertainty. The fits use the full systematic error matrix and all have acceptable χ^2; the resulting ξ^* values are listed in Table III with their total uncertainties. The statistical uncertainties are negligible, and the RMS uncertainties are small except for the $\pi^\pm$, where they are about half the other systematics. Adding more ranges to any set of fits has little effect on the results.

To test the prediction regarding the Gaussian shape, we first find the largest range centered near ξ^* over which the Gaussian fit is acceptable, i.e., yields a χ^2 with a confidence level exceeding 0.01. We then extend the fit range to either lower or higher values, if possible, to find a maximum range over which this function gives an acceptable fit. These ranges are listed in Table IV and the fits are shown as
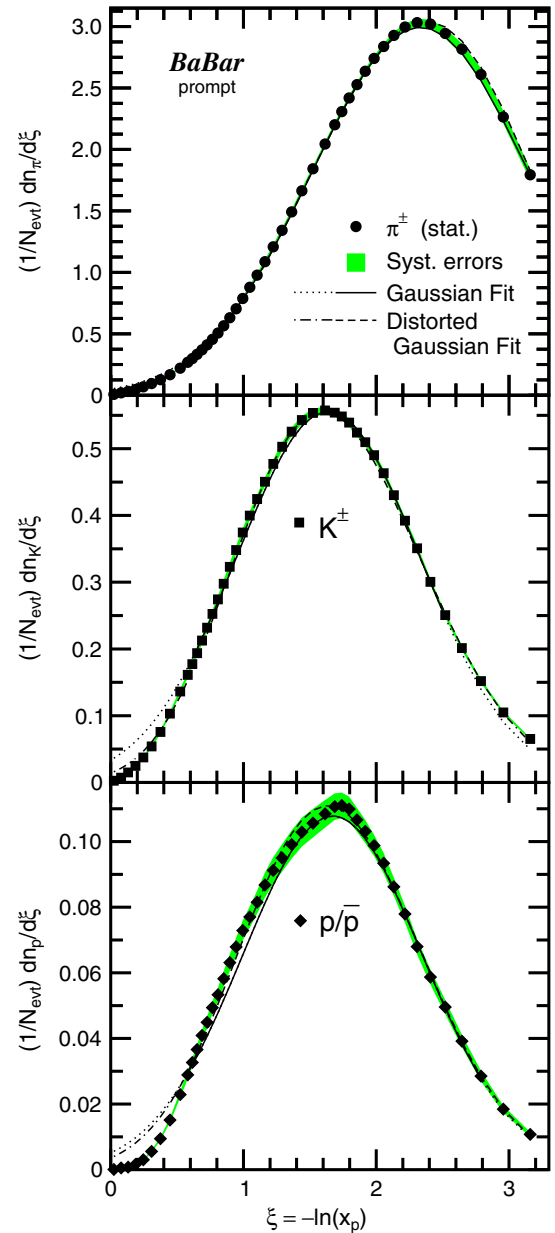

FIG. 15 (color online). Differential cross sections in ξ for prompt $\pi^\pm$ (top), $K^\pm$ (middle), and $p/\bar{p}$ (bottom). The error bars are statistical only, and the gray bands represent the systematic uncertainties, which are strongly correlated from point to point. Also shown are the results of the Gaussian (solid lines) and distorted Gaussian (dashed lines) fits described in the text over their maximum ranges (see Table IV); they are continued as dotted and dot-dashed lines, respectively, outside those ranges.

the lines on Fig. 15. In each case we obtain a good fit over a range more than one unit wide, consistent with the prediction. For $K^\pm$ and $p/\bar{p}$ the maximum ranges are centered near the peak and span nearly two units in width. The maximum range for pions extends to the end of our coverage, which is just under one unit above the peak. It extends more than 1.5 units below the peak, but data at higher ξ might constrain this more tightly.

TABLE III.   Peak positions ξ^*, determined as described in the text, with total uncertainties, which are dominated by systematic terms.

	$\pi^\pm$	$K^\pm$	$p/\bar{p}$
Prompt	2.337 ± 0.009	1.622 ± 0.006	1.647 ± 0.019
Conventional	2.353 ± 0.009	1.622 ± 0.006	1.604 ± 0.013

TABLE IV.   Maximum ranges over which we obtain good fits using a simple Gaussian function and a distorted Gaussian function that includes skewness and kurtosis terms.

	Prompt		Conventional	
Hadron	Gaussian	Distorted	Gaussian	Distorted
$\pi^\pm$	0.92–3.27	0.22–3.27	0.87–3.27	0.67–3.27
$K^\pm$	0.63–2.58	0.34–3.05	0.63–2.58	0.34–3.05
$p/\bar{p}$	0.56–3.27	0.48–3.27	0.71–2.58	0.48–3.27

FIG. 16 (color online).   Peak positions ξ^* vs CM energy for pions (circles), kaons (squares) and protons (diamonds) on a logarithmic horizontal scale. The lines join our points with those from the averages of the Z^0 experiments.

Next, we add approximate skewness (s) and kurtosis (κ) terms to our fitting function, following Ref. [42]:

$$G'(\xi) = \frac{N}{\sigma\sqrt{2\pi}} \exp\left(\frac{\kappa}{8} + \frac{s\delta}{2} - \frac{(2+\kappa)\delta^2}{4} + \frac{s\delta^3}{6} + \frac{\kappa\delta^4}{24}\right),$$

where $\delta = (\xi - \xi^*)/\sigma$, and σ is the standard deviation. We repeat the exercise of finding the maximum ξ range for which a fit of this function is acceptable. The results are listed in Table IV and shown as the dashed lines on Fig. 15. The prompt (conventional) $\pi^\pm$ range can be extended to substantially (somewhat) lower ξ values, consistent with the prediction. However, the fitted skewness and kurtosis values increase rapidly as the range is extended, to -0.37 (-0.11) and -0.43 (-0.30), respectively, at the widest range, and it is unknown how additional data on the high side of the peak might affect the fits. The $K^\pm$ and $p/\bar{p}$ ranges can be extended somewhat in both directions with

similar s and κ values. Given our relatively low E_{CM} and hence narrow ξ range, this should also be considered consistent with the prediction.

We find ξ^*_π to be 0.8 units higher than ξ^*_K, consistent with the predicted decrease with hadron mass, but ξ^*_p is not lower than ξ^*_K. This is similar to the behavior observed at higher energies where mesons and baryons appear to follow different trajectories, but measurements for more particles at our E_{CM} would be needed to draw firm conclusions. In Fig. 16 we show a compilation of ξ^* measurements for $\pi^\pm$, $K^\pm$ and $p/\bar{p}$ as a function of CM energy. Our precise values and those from the Z^0 provide strong constraints on the trajectories, and the lines on the plot simply join the points at these two energies. The other data are consistent with the lines, and hence with the predicted energy dependence, but more precise data at other energies are needed to test the form of the increase. The slopes of the lines for pions and protons are similar, but that for the

TABLE V.   Integrated measured cross sections, the fractional coverage estimated as described in the text, and the fully corrected $e^+e^- \to q\bar{q}$ event multiplicities from this measurement. The first error on the yield is experimental, dominated by systematics, and the second is from the uncertainty on the coverage. The other columns show previous results from the CLEO [33] and ARGUS [11] experiments, and values predicted by the models described in the text.

			Yield per $q\bar{q}$ event					
Particle	Measured integral	Coverage	*BABAR*	CLEO	ARGUS	JETSET	UCLA	HERWIG
Prompt								
$(e\mu\pi)^\pm$	5.51 ± 0.08	0.876 ± 0.018	$6.29 \pm 0.09 \pm 0.13$			5.84	5.88	5.73
$\pi^\pm$	5.36 ± 0.08	0.884 ± 0.019	$6.07 \pm 0.09 \pm 0.13$		5.694 ± 0.108	5.59	5.62	5.49
$K^\pm$	0.946 ± 0.012	0.973 ± 0.016	$0.972 \pm 0.012 \pm 0.016$		0.888 ± 0.030	1.01	1.02	1.01
$p/\bar{p}$	0.182 ± 0.006	0.984 ± 0.007	$0.185 \pm 0.006 \pm 0.001$		0.212 ± 0.017	0.28	0.14	0.31
Conventional								
$(e\mu\pi)^\pm$	6.15 ± 0.10	0.867 ± 0.019	$7.09 \pm 0.11 \pm 0.16$			6.58	6.60	6.55
$\pi^\pm$	6.00 ± 0.10	0.874 ± 0.020	$6.87 \pm 0.11 \pm 0.16$	8.3 ± 0.4	6.38 ± 0.12	6.33	6.34	6.31
$K^\pm$	0.946 ± 0.012	0.973 ± 0.016	$0.972 \pm 0.012 \pm 0.016$	1.3 ± 0.2	0.888 ± 0.030	1.01	1.02	1.01
$p/\bar{p}$	0.261 ± 0.008	0.984 ± 0.008	$0.265 \pm 0.008 \pm 0.002$	0.40 ± 0.06	0.271 ± 0.018	0.37	0.20	0.46

kaons is quite different. This could be due to the changing flavor composition.

D. Average multiplicities, ratios and fractions

To estimate the average numbers of pions, kaons and protons produced per event, we integrate the differential cross sections over the measured p^* range, and correct for the unmeasured parts of the spectra. The integrals take all systematic uncertainties and their correlations into account, and are listed in the second column of Table V. The uncertainties are dominated by the normalization and fully correlated tracking systematics; there are also substantial contributions to the conventional $\pi^\pm$ and $p/\bar{p}$ results from the K_S^0 and strange baryon cross sections.

From Fig. 15, it is clear that the coverage, i.e. the fraction of the spectrum covered by our measurement, is over 95% for $K^\pm$ and $p/\bar{p}$. However, it is smaller for $\pi^\pm$, and in no case is it clear *a priori* how to account for this reliably. We consider four estimates of our coverage, one from each of the three hadronization models and one from an ensemble of distorted Gaussian fits. We consider fits over all ranges that include the ten highest-ξ points and give an acceptable χ^2 calculated from only the bins above the peak plus the five bins just below the peak. The average of these four coverage values is given in the third column of Table V, with an uncertainty that corresponds to their RMS deviation. The spread among the fits is smaller than this, as are variations obtained by running any simulation with different parameter values. We divide each measured integral by the corresponding coverage to obtain the average event multiplicity listed in column four of Table V.

Previous results from CLEO at 10.49 GeV [33] and ARGUS at 9.98 GeV are also listed in Table V, as are the predictions of the three hadronization models. Our prompt (conventional) $\pi^\pm$ rate is 7% (8%) and 2.0σ (2.2σ) higher than the ARGUS rate. A difference of this size is expected from the E_{CM} difference. Our $K^\pm$ and $p/\bar{p}$ rates are also slightly higher than the ARGUS rates. The CLEO rates are substantially higher than ours, but their uncertainties are large. With default parameter values, all three models give conventional $\pi^\pm$ rates close to the ARGUS value and 8%–9% below ours, even though the simulations are run at our E_{CM}. The models predict $K^\pm$ rates that are slightly too high, and widely varying $p/\bar{p}$ rates, none of which is consistent with the data. The total charged hadron rates from ARGUS and CLEO are among the main inputs to the tuning of these models.

From our cross sections we can derive production ratios for pairs of hadrons, in which many of the systematic uncertainties cancel at least partly. The remaining uncertainties are dominated by particle identification systematics. Previous experiments have presented this information in the form of the fractions of all charged hadrons that are pions, kaons and protons, f_π, f_K and f_p. We show our fractions for prompt and conventional hadrons in Fig. 17,
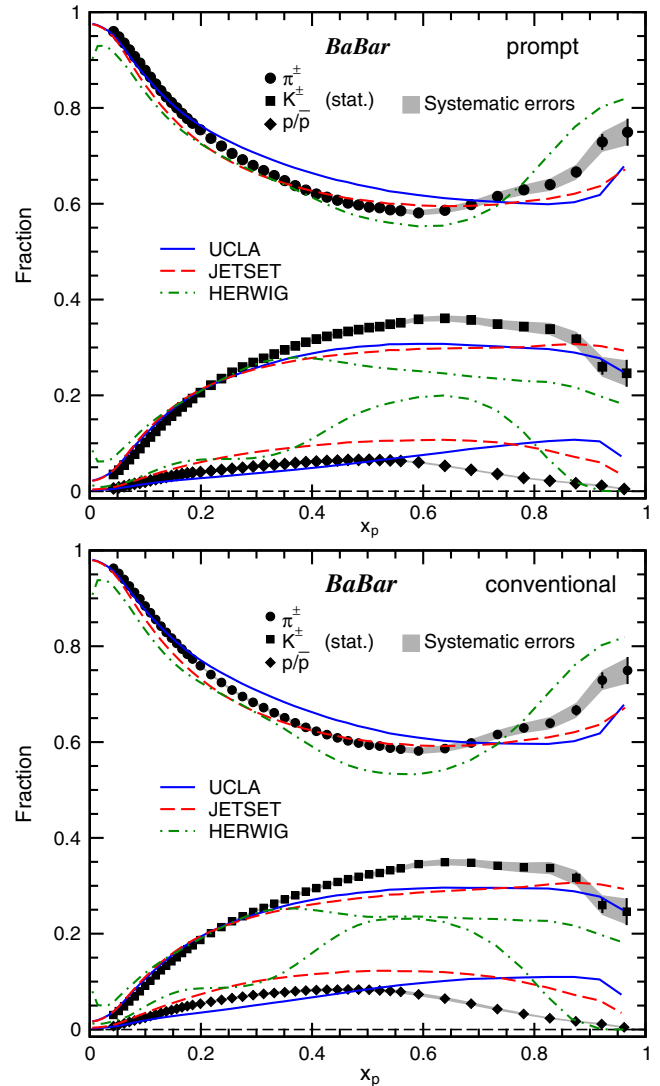

FIG. 17 (color online).   Prompt (top) and conventional (bottom) $\pi^\pm$, $K^\pm$, and $p/\bar{p}$ fractions. The error bars are statistical only, and the gray bands represent the systematic uncertainties, which are strongly correlated from point to point. Also shown are the predictions of the three hadronization models.

and tabulate them in the Supplemental Material [38]. The prompt and conventional fractions are quite similar, and converge at high x_p. Strange hadron decay products cause the conventional f_π and f_p to be larger than their prompt counterparts at low x_p, with f_K correspondingly smaller.

The dominance of pions at low x_p is expected due to their lower mass and the contributions from decays of heavier hadrons. The plateau values of f_K and f_p near $x_p = 0.6$, of about 0.35 and 0.08, respectively, might reflect the intrinsic relative production of strange particles and baryons in the hadronization process. The decrease of f_p at high x_p might be kinematic—a proton must be produced along with an antibaryon, and the mass of the pair is a large fraction of $E_{CM}/2$. The $K^\pm$ from $c\bar{c}$ events are also

kinematically limited, whereas those from $s\bar{s}$ and $u\bar{u}$ events become more important as x_p increases, until perhaps the very highest-x_p bins.

The predictions of the three models are also shown, and do not describe the data well. JETSET and UCLA provide reasonable qualitative descriptions but underpredict f_K and overpredict f_p at high x_p. In particular f_p does not decrease early or quickly enough. HERWIG's description of f_p is poor, and this affects f_π and f_K, which might otherwise be described reasonably well.

VII. SUMMARY

We present measurements of the differential production cross sections for charged pions, kaons, and protons in e^+e^- annihilations at $E_{CM} = 10.54$ GeV, both excluding (prompt) and including (conventional) decay products of K_S^0 mesons and weakly decaying strange baryons. The measurements cover the CM momentum (p^*) range from 0.2 GeV/c to the beam momentum. Comparing with previous measurements at the nearby E_{CM} of 9.98 GeV, we find consistency for p^* in the 1–3 GeV/c range, and evidence for scaling violations below 1 GeV/c.

These data can be used to test and tune models of the hadronization process. We find that the JETSET, UCLA, and HERWIG models, which were tuned to previous data between 9.98 and 35 GeV, reproduce the $\pi^\pm$ and $K^\pm$ spectra to within 15% over most of the p^* range, but do not describe their shapes in detail. All three models provide poor descriptions of the $p/\bar{p}$ spectra. Comparing the same models with data at higher E_{CM}, we find that they reproduce the high-p^* scaling properties of the $\pi^\pm$ cross section to within a few percent and the $K^\pm$ spectrum to within 15%, but predict about twice the scaling violation observed for $p/\bar{p}$.

The shape of the $\xi = -\ln(x_p)$ spectrum predicted by MLLA QCD is consistent with our data in all cases, and the peak positions ξ^* are lower for $K^\pm$ than $\pi^\pm$, as predicted. However, the ξ^* for $p/\bar{p}$ are not lower than those for $K^\pm$. This is consistent with the behavior observed at higher E_{CM}, where the predicted mass dependence holds for

mesons and baryons separately, but not together. The predicted E_{CM} dependence is consistent with the world's data, with the slopes being similar for $\pi^\pm$ and $p/\bar{p}$; the $K^\pm$ slope is lower, perhaps due to the changing flavor composition with increasing E_{CM}.

We integrate over the measured p^* ranges, and extrapolate into the unmeasured regions, to measure a total of 6.07 ± 0.16, 0.97 ± 0.02, and 0.19 ± 0.01 prompt (6.87 ± 0.19, 0.97 ± 0.02, and 0.27 ± 0.01 conventional) $\pi^\pm$, $K^\pm$ and $p/\bar{p}$, respectively, per hadronic event. We also provide hadron fractions, in which many of the systematic uncertainties cancel. These measurements are also consistent with previous results and provide additional information that can be used to test models.

[1] See, e.g., R. K. Ellis, D. A. Ross, and A. E. Terrano, Nucl. Phys. **B178**, 421 (1981).

[2] See, e.g., S. Moretti, Phys. Lett. B **420**, 367 (1998).

[3] Y. I. Azimov, Y. L. Dokshitzer, V. A. Khoze, and S. I. Troian, Z. Phys. C **27**, 65 (1985).

[4] G. Marchesini and B. R. Webber, Nucl. Phys. **B238**, 1 (1984).

[5] S. Albino, B. A. Kniehl, and G. Kramer, Nucl. Phys. **B803**, 42 (2008); D. de Florian, R. Sassot, and M. Stratmann, Phys. Rev. D **75**, 114010 (2007); M. Hirai, S. Kumano,

T. H. Nagai, and K. Sudoh, Phys. Rev. D **75**, 094009 (2007).

[6] See, e.g., A. Böhrer, Phys. Rep. **291**, 107 (1997); G. D. Lafferty, P. J. Reeves, and M. R. Whalley, J. Phys. G **21**, A1 (1995); D. H. Saxon, in *High Energy Electron-Positron Physics*, edited by A. Ali and P. Söding (World Scientific, Singapore, 1988), Vol. 1, p. 539.

[7] G. Corcella, I. G. Knowles, G. Marchesini, S. Moretti, K. Odagiri, P. Richardson, M. H. Seymour, and B. R. Webber, J. High Energy Phys. 01 (2001) 010;

G. Marchesini, B. R. Webber, G. Abbiendi, I. G. Knowles, M. H. Seymour, and L. Stanco, Comput. Phys. Commun. **67**, 465 (1992).

[8] T. Sjöstrand, Comput. Phys. Commun. **82**, 74 (1994).

[9] S. Chun and C. Buchanan, Phys. Rep. **292**, 239 (1998).

[10] P. Abreu *et al.* (DELPHI Collaboration), Phys. Lett. B **398**, 194 (1997).

[11] H. Albrecht *et al.* (ARGUS Collaboration), Z. Phys. C **44**, 547 (1989).

[12] H. Aihara *et al.* (TPC-2Gamma Collaboration), Phys. Rev. Lett. **61**, 1263 (1988).

[13] W. Braunschweig *et al.* (TASSO Collaboration), Z. Phys. C **42**, 189 (1989).

[14] R. Itoh *et al.* (TOPAZ Collaboration), Phys. Lett. B **345**, 335 (1995).

[15] P. Abreu *et al.* (DELPHI Collaboration), Eur. Phys. J. C **5**, 585 (1998).

[16] R. Akers *et al.* (OPAL Collaboration), Z. Phys. C **63**, 181 (1994).

[17] D. Buskulic *et al.* (ALEPH Collaboration), Z. Phys. C **66**, 355 (1995).

[18] K. Abe *et al.* (SLD Collaboration), Phys. Rev. D **59**, 052001 (1999); **69**, 072003 (2004).

[19] P. Abreu *et al.* (DELPHI Collaboration), Eur. Phys. J. C **18**, 203 (2000); **25**, 493(E) (2002).

[20] M. Leitgab *et al.* (Belle Collaboration), Phys. Rev. Lett. (to be published).

[21] K. Abe *et al.* (SLD Collaboration), Phys. Rev. Lett. **78**, 3442 (1997); **79**, 959(E) (1997).

[22] G. Abbiendi *et al.* (OPAL Collaboration), Eur. Phys. J. C **16**, 407 (2000).

[23] B. Aubert *et al.* (*BABAR* Collaboration), Nucl. Instrum. Methods Phys. Res., Sect. A **479**, 1 (2002); arXiv:1305.3560.

[24] I. Adam *et al.* (*BABAR* DIRC Collaboration), Nucl. Instrum. Methods Phys. Res., Sect. A **538**, 281 (2005).

[25] G. C. Fox and S. Wolfram, Phys. Rev. Lett. **41**, 1581 (1978); Nucl. Phys. **B149**, 413 (1979).

[26] S. Brandt, Ch. Peyrou, R. Sosnowski, and A. Wroblewski, Phys. Lett. **12**, 57 (1964); E. Farhi, Phys. Rev. Lett. **39**, 1587 (1977).

[27] S. Agostinelli *et al.* (GEANT4 Collaboration), Nucl. Instrum. Methods Phys. Res., Sect. A **506**, 250 (2003).

[28] S. Jadach and Z. Was, Comput. Phys. Commun. **64**, 267 (1991).

[29] J. Beringer *et al.* (Particle Data Group), Phys. Rev. D **86**, 010001 (2012).

[30] S. Jadach, W. Placzek, and B. F. L. Ward, Phys. Lett. B **390**, 298 (1997).

[31] H. Czyz and J. H. Kühn, Eur. Phys. J. C **18**, 497 (2001).

[32] H. Paar and M. Sivertz (to be published); based on V. M. Budnev, I. F. Ginzburg, G. V. Meledin, and V. G. Serbo, Phys. Rep. **15**, 181 (1975).

[33] S. Behrends *et al.* (CLEO Collaboration), Phys. Rev. D **31**, 2161 (1985); H. Albrecht *et al.* (ARGUS Collaboration), Z. Phys. C **62**, 371 (1994).

[34] B. L. Hartfiel, Ph.D. thesis, University of California-Los Angeles [Institution Report No. SLAC-R-823, 2004 (unpublished)].

[35] T. Allmendinger *et al.*, Nucl. Instrum. Methods Phys. Res., Sect. A **704**, 44 (2013).

[36] S. Christ, Ph.D. thesis, Universität Rostock, 2003 (unpublished).

[37] B. Aubert *et al.* (*BABAR* Collaboration), Phys. Rev. D **72**, 052006 (2005).

[38] See Supplemental Material at http://link.aps.org/supplemental/10.1103/PhysRevD.88.032011 for tables of charged hadron fractions, uncertainties and correlation matrices.

[39] M. Artuso *et al.* (CLEO Collaboration), Phys. Rev. D **70**, 112001 (2004).

[40] R. Seuster *et al.* (Belle Collaboration), Phys. Rev. D **73**, 032002 (2006).

[41] B. Aubert *et al.* (*BABAR* Collaboration), Phys. Rev. D **75**, 012003 (2007).

[42] Y. L. Dokshitzer, V. A. Khoze, and S. I. Troian, Int. J. Mod. Phys. A **07**, 1875 (1992); C. P. Fong and B. R. Webber, Phys. Lett. B **229**, 289 (1989).